1	Seasonal Asymmetry of Equatorial East African Rainfall Projections: Understanding
2	Differences between the Response of the Long Rains and the Short Rains to Increased
3	Greenhouse Gases
4	
5	Kerry H. Cook <sup>1</sup> , Rory G. J. Fitzpatrick <sup>1</sup> , Weiran Liu <sup>1,2</sup> , and Edward K. Vizy <sup>1</sup>
6	
7	<sup>1</sup> Department of Geological Sciences, University of Texas at Austin, Austin TX, USA
8	<sup>2</sup> Current affiliation: University of California at Davis, Davis CA
9	
10	
11	
12	
13	Citation: Cook, K.H., Fitzpatrick, R.G.J., Liu, W., Vizy, E.K. Seasonal asymmetry of
14	equatorial East African rainfall projections: understanding differences between the response of
15	the long rains and the short rains to increased greenhouse gases. Clim Dyn (2020).
16	https://doi.org/10.1007/s00382-020-05350-y
17	
18	
19	
20	Corresponding author address: kc@jsg.utexas.edu
21	

#### Abstract

Ensemble simulations with a regional climate model on a large domain and 30-km resolution are used to understand why projected precipitation changes under greenhouse gasforcing are asymmetric across seasons in equatorial East Africa, with rainfall increasing during the short rains (October through December) but not during the long rains (March through May). The model captures an accurate simulation of observed East African precipitation improving over coupled GCM simulations. Future simulations are generated by increasing atmospheric CO<sub>2</sub> according to the RCP8.5 scenario and adding anomalies to observed SSTs as well as initial and lateral boundary conditions derived from coupled GCM simulations.

In November, simulated rainfall rates increase by approximately one-third over much of equatorial East Africa by the mid-21<sup>st</sup> century, and double by the end of the century. The long rains are not significantly increased. The difference in the seasonal response is attributed to differences in the background state. The East African short rains are greatest in November, more than one month after the autumnal equinox, when the climatological basic state is in a solstitial pattern. The well-defined heat low over southern Africa and the South Indian Ocean subtropical high to its east are intensified, leading to enhanced moisture convergence over equatorial East Africa. In contrast, the long rains are near their maximum on the vernal equinox, with a continental thermal low centered near the equator that is insensitive to 21<sup>st</sup> century greenhouse gas-induced changes in the subtropical atmospheric hydrodynamics.

- Keywords: East Africa; East African precipitation; East Africa precipitation trends; Angola
- Low; Mascarene High; South Indian high; East Africa precipitation projections; East African
- 44 climate change projections; East African long rains; East African short rains; Turkana
- 45 channel

#### 1. Introduction

Precipitation over East Africa is bimodal over large regions, with a boreal spring rainy season in March through mid-May known as the long rains, and a late-fall rainy season in October through December known as the short rains. Some analyses of observations over the late 20<sup>th</sup> and early 21<sup>st</sup> centuries suggest that there is a decreasing trend in rainfall during the long rains, while other studies do not find a trend. Rainfall totals delivered during the short rains season have increased. The implication is that these asymmetric trends are being forced by increasing atmospheric greenhouse gas levels, but a poor representation of the East African rainy seasons and their modes of natural variability in coupled GCMs (CGCMs) undermines confidence in our ability to use these models for projection and attribution of change on this regional space scale.

Here we analyze the response of the East African long and short rains to increasing atmospheric greenhouse gases using regional climate model simulations that were performed using a large domain – including all of Africa and the surrounding oceans - with 30-km resolution. In the ensemble simulations, greenhouse gas forcing is applied by increasing atmospheric CO<sub>2</sub> in the model, and also by adding anomalies derived from CGCM simulations to observed SSTs. This simulation design provides an improved simulation of the East African rainy seasons compared with CGCMs because of the improved representation of the region's complex topography, realistic SST distributions, and customized physical parameterizations choices.

Section 2 provides background on the climatology of East African rainfall, and its observed and projected trends. In section 3 we discuss the model ensemble simulations and the evaluation of confidence in the projections along with the observational datasets and analysis methodology employed. Model evaluation is in section 4, followed by an analysis that explains

why the seasonal rainfall projections for the long rains and short rains are different. Section 5 provides concluding remarks.

### 2. Background

East Africa stretches across 40° degrees of latitude, from the Horn of Africa (Ethiopia, Eritrea, Djibouti, and Somalia), through the equatorial region (Kenya, Uganda, Rwanda, Burundi, South Sudan, and Tanzania), to Mozambique and Malawi in the south. The presence of two rainy seasons is common, especially in equatorial East Africa within 10° of the equator, which is the focus of this paper. One rainy season, the "long rains", typically lasts from March through May, and the "short rains" season occurs in October through December. These rainy seasons develop in the absence of strong meridional flow associated with the Somali jet in Northern Hemisphere summer and its reversal in winter (Vizy and Cook 2020), contradicting the idea that the rainfall seasonality is determined by the seasonal excursions of the intertropical convergence zone.

During the long rains, onshore flow carries moisture from the South Indian Ocean that is channeled into equatorial East Africa by the topography, and strong moisture flux through the orographic gap known as the Turkana Channel (5°N, 36°E) supports rainfall in the interior (Nicholson 2016; Hartman 2018; Vizy and Cook 2019). The onshore transport of high moist static energy from the warm western Indian Ocean overcomes the divergence of the overlying air to produce the rainy season (Yang et al. 2015). Interannual variability of the long rains is smaller than that of the short rains. Connections to remote SST forcing during the long rains season are weak (Ogallo et al 1988; Mutai and Ward 2000), and their prediction on seasonal and even intraseasonal time scales exhibits low skill (Dutra et al 2013; Nicholson 2014; MacLeod 2019).

A number of observational studies indicate a negative trend in the long rains precipitation, primarily over the 1980-2010 period (Lyon and DeWitt 2012; Funk et al. 2015; Rowell et al., 2015; Maidment et al. 2015; Ongoma and Chen 2017; Cattani et al., 2018). Many different averaging regions are used in these studies, and analyses do not agree about the causes of the suggested decline. Natural variability, greenhouse gas increases (Williams and Funk 2011; Liebmann et al. 2014; Yang et al. 2014), western Pacific SST forcing (Liebmann et al. 2017), and the Pacific Decadal Oscillation (Omondi et al. 2013) have all been implicated. Wainwright et al. (2019) suggest that the drying signal is associated with a shortening of the long-rains season, consistent with the modeling study of Cook and Vizy (2013). Recent studies suggest that the drying primarily occurred during the 1998-2009 period, was highly regional, and did not persist into the second decade of the 21st c. (Wainwright et al. 2019, Cook and Vizy 2019). Kenya has experienced record-breaking spring rains recently, for example (Kilavi 2018).

Unlike the long rains, the short rains exhibit substantial sensitivity to SSTAs and, as a result, they are more variable than the long rains (Nicholson 2014; Ndomeni et al. 2018) and seasonal prediction may hold more promise (e.g., Lu et al. 2016). Studies of the connection between SSTA and the short rains fall roughly into two types. In one, the intensity of the East African short rains is related to SST gradients across the Indian Ocean, referred to as the Indian Ocean Dipole (IOD) or the Indian Ocean Zonal Mode (IOZM). Different authors use different averaging periods and various means of measuring the zonal SST gradient and its variations (e.g., Saji and Yamagata 2003, Behera et al 2005). Black et al. (2003) indicate that the relationship is confined primarily to extreme IOZM years, which are coupled with ENSO (see also Bahaga et al. (2019).

The other type of study finds that the sensitivity of the East African short rains to Indian Ocean SSTs is dominated by a sensitivity to western Indian Ocean SSTAs, rather than to zonal

SST gradient. Bahaga et al. (2015) evaluate the predictability of the East African short rains in observations and find a dominant role for the western Indian Ocean, when warm anomalies induce a Gill-type response to steady equatorial heating. Atmosphere-only model studies by Ummenhofer et al. (2009) and Liu et al. (2020), with SSTAs imposed individually in various regions of the Indian Ocean, support this result. They explicitly show that there is only weak direct influence on the East African short rains from SSTAs in the central and eastern Indian Ocean.

In contrast to the long rains, recent observations suggest that precipitation during the short rains is increasing (Gebrechorkos et al. 2019). Cattani et al. (2018) examine three satellite-based time series for 1983-2015 and find wide-spread precipitation increases in October through December over East Africa, excepting a region over Kenya.

A poor representation of the equatorial East African rainy seasons in coupled GCMs has been reported and analyzed (e.g., Otieno and Anya 2013; Dunning et al. 2017; Ongoma et al. 2019), adding to uncertainty in the projections. These models simulate very weak long-rains precipitation and produce rainfall that is too strong during the short rains season (Otieno and Anya 2013; Yang et al. 2015; Rowell et al. 2015). Consistent with the strong connection between East African rainfall and Indian Ocean SSTs, these studies find that inaccuracies in the simulations of East Africa rainfall are at least partly associated with the ocean component of the CGCMs. For example, Ummenhofer et al. (2018) use natural variability as a proxy for evaluating responses to SSTs in a coupled GCM, and find that the modeled long rains exhibit spurious responses to remote SST forcing such as ENSO. Atmosphere-only GCMs, with realistic SSTs prescribed, produce improved simulations of the rainy seasons (see Fig. 5 in Cook and Vizy 2019). With prescribed SSTs and resolution better able to accurately capture the complex topography of East Africa, regional models also are able to improve on CGCM simulations (Endris et al. 2013; Cook and Vizy 2013; Han et al. 2019). Additional

improvements that include a correct simulation of the diurnal cycle of rainfall come from convective-permitting modeling (Finney et al. 2019).

In summary, past research makes it clear that variability and trends of the long rains and the short rains are significantly different from each other. Here we focus on greenhouse gas-induced trends. The hydrodynamics of the changes in precipitation during each season are analyzed using a high-resolution, ensemble modeling approach to understand the fundamental reasons for the differences in behavior between the two rainy seasons.

### 3. Data and methods

#### 3.1 Ensemble model simulations

Simulations of the late 20<sup>th</sup> century, mid-21<sup>st</sup> century, and late 21<sup>st</sup> century created using the Weather Research and Forecasting model V3.1.1 (WRF; Skamarock et al., 2008) are used to project changes over East Africa due to increasing atmospheric greenhouse gas levels. A nested-domain configuration is used, with 90-km resolution over the outer domain and 30-km resolution over the inner domain (Figure 1). There are 32 vertical levels in the simulations, and the top of the atmosphere is set at 20 hPa. The choice of large domain is deliberate, to reduce the influence of lateral boundary conditions on the model's interior solution (Cook and Vizy, 2006).

Model parameterizations employed include the Yonsei University planetary boundary layer (Hong et al. 2006), Monin-Obukhov surface layer, new Kain-Fritsch cumulus convection (Kain 2004), Purdue Lin microphysics (Chen and Sun 2002), RRTM longwave radiation (Mlawer et al., 1997), Dudhia shortwave radiation (Dudhia 1989), and the unified Noah land surface model (Chen and Dudhia 2001). These parameterizations were tested for the time scales and domains of these simulations, and have previously been shown to yield a realistic

representation of the African climate (Vizy and Cook 2012; Cook and Vizy 2012; Vizy et al. 2013).

Three 20-member ensemble simulations are used. One is a control simulation, called LATE20, which runs from 1989 to 2008 to match the last 20 years of the CMIP5 historical runs. The twenty years of this simulation are used as a 20-member ensemble. Initial, lateral, SST, and surface boundary conditions are interpolated and applied every 6 hours from the National Centers for Environmental Prediction reanalysis 2 (NCEP2; Kanamitsu et al. 2002), and atmospheric CO<sub>2</sub> is set to the average observed level of 367 ppmv for this time period.

A second 20-member ensemble, MID21, represents the mid-21<sup>st</sup> century (2041-206) with CO<sub>2</sub> emissions increased to 546 ppmv according to the Intergovernmental Panel on Climate Change AR5 Regional Climate Pathway 8.5 scenario (RCP8.5). While this scenario for CO<sub>2</sub> emissions is seen as quite steep by some energy analysts (e.g., Ritchie and Dowlatabadi 2017), we use it to produce perturbations that can be cleanly analyzed and to account for not including emissions of other greenhouse gases such as methane. In addition to increased CO<sub>2</sub>, mid-21<sup>st</sup> c. conditions are imposed by adding SSTAs to the observed values and perturbing initial and lateral boundary conditions. All of these anomalies are derived from multiple CMIP5 simulations. This methodology was first developed by Cook and Vizy (2006) and Patricola and Cook (2007), and it is detailed for these simulations in Vizy et al. (2013). The use of multiple CMIP5 models reduces the dependence of the future simulation on the quality of a single CMIP5 model as can occur when downscaling. Applying GCM-derived anomalies to observed SSTs, rather than directly using GCM-generated SSTs, avoids propagating errors in the simulation of SSTs into the regional model simulation and preserves a level of independence of the regional simulation to add value to comparisons with GCM solutions.

The third ensemble, LATE21, represents 2081-2100 with CO<sub>2</sub> at 850 ppmv, and SST and boundary-condition anomaly forcing again derived from analogous coupled CMIP5 GCM

simulations. In the course of the model integration, deepening of the troposphere and intensification of convection produced hydrodynamics instability on the 30-km domain, and only 9 ensemble members could be produced. (Note that this instability in the regional model is avoided by setting the top of the atmosphere to a lower pressure level than has been customary.) The full 20-year integration was completed with the 90-km domain to provide a check on the 9-member ensemble analyzed here.

Confidence in the model projections is supported by comparing the LATE20 simulation with the observed climatology of the same period, and we are also able to include some limited comparison with still-emerging observed trends. In addition, the ensemble simulation design allows for the calculation of statistical significance. Finally, the analysis of the simulated climate change trends is taken to the process level. Developing a physical understanding of the simulated changes and their relationships to the greenhouse gas forcing allows us to evaluate whether the perturbation to the climate is convincing.

# 3.2 Observational and reanalysis datasets

- To evaluate the LATE20 model simulation over East Africa, observational datasets with relatively high resolution that have been used successfully in other studies as reviewed above are chosen. The following four observational precipitation products are used:
  - NASA TRMM 3B42 V7 Precipitation (Huffman et al. 2007): A 0.25° resolution, multi-satellite precipitation analysis (TMPA) with 3-hourly rainfall estimates between 50°S 50°N from January 1998 to present.
    - The NOAA Climate Prediction Center morphing technique precipitation V2 biascorrected dataset (CMORPH; Joyce et al. 2004; Xie et al. 2017). 8-km resolution precipitation providing estimates every 30 min for 1998–present using satellite passive microwave and infrared measurements.

- The Climate Hazards Group Infrared Precipitation with Satellite Data (CHIRPS2; Funk et al. 2015). Estimates are available for 1981-present at 0.05° resolution from satellite infrared measurements from 50°S to 50°N combined with in-situ station data.
  - Precipitation Estimation from Remotely Sensed Information using Artificial Neural Networks – Climate Data Record (PERSIANN; Ashouri et al. 2015). Daily estimates at 0.25° resolution for 1983-present based on GridSat-B1 infrared satellite data combined with an artificial neural network trained on hourly precipitation.

Simulated atmospheric circulation and moisture fields are evaluated by comparing with the European Centre for Medium Range Weather Forecasting ERA5 reanalysis dataset (ERA5 2018). The 31-km resolution of the ERA5 reanalysis is close to that of the model simulations and produces a realistic representation of the topography and low-level circulation of the region, including the Turkana Jet (Vizy and Cook 2019).

### 3.3 Moisture budget analysis

An analysis of the atmospheric water vapor budget is used to relate precipitation anomalies in the simulations to changes in circulation and atmospheric water vapor distributions. For the climatological average, over which the time rate of change of the specific humidity, q, is zero, conservation of water mass in an atmospheric column requires that precipitation is balanced by the combination of evaporation and the vertically-integrated moisture flux convergence according to

$$\overline{P} = \overline{E} - \left( \frac{1}{\rho_w g} \int_{\rho_s}^{0} \nabla \cdot (q \vec{r}) dr \right)$$
 (1)

where P is precipitation, E is evapotranspiration, g is gravitational acceleration,  $\rho_{\omega}$  is the density of water,  $\rho_{s}$  is the surface pressure,  $\vec{r}$  is the horizontal wind vector, and the overbars

indicate a climatological mean. We decompose the vertically-integrated moisture convergence term into a convergence term, *C*, an advective term, *A*, and a residual, *R*, defined by

$$C = -\frac{1}{g\overline{\rho}_{w}} \int_{p_{s}}^{0} \overline{q} \nabla \cdot (\vec{r}_{j}, \vec{r}_{k}), \qquad (2)$$

$$A = -\frac{1}{g\overline{\rho}_w} \int_{p_s}^{0} \overline{r} \, dr \, , \qquad (3)$$

246 and

$$R = P - E - C - A. \tag{4}$$

248 *R* includes orographic precipitation, the effects of transient eddies, and numerical error (Lenters 249 and Cook 1995; Vizy and Cook 2002; Patricola and Cook 2011; Cook and Vizy 2013). The 250 convergence term is further decomposed into zonal and meridional convergence terms. In the 251 vertical integral, these terms are given by

$$C_{Z} = -\frac{1}{g\bar{\rho}_{w}} \int_{p_{w}}^{0} \bar{q} \, \frac{\partial \bar{u}}{\partial x} dp \tag{5}$$

253 and

$$C_{M} = -\frac{1}{g\overline{\rho}_{w}} \int_{p_{s}}^{0} \overline{q} \frac{\partial v}{\partial y} dp.$$
 (6)

255 Moisture budget terms are also evaluated on individual pressure levels.

257 *4. Results* 

256

258

259

260

261

# 4.1 Evaluation of the LATE20 simulation

Since our analysis is focused on comparing and contrasting projected changes in the two rainy seasons that characterize rainfall seasonality over a large portion of East Africa, the model evaluation here is largely restricted to those seasons. For additional evaluation of these simulations, please see Vizy et al. (2013), Busby et al. (2014), Vizy et al. (2015), and Han et al. (2019).

Figure 2a displays 10-day smoothed climatological daily precipitation rates averaged over land from 30 – 50°E and 10°S – 5°N in the LATE20 simulation and four observational datasets. According to the observational datasets, the long rains begin in March, peak in April, and decline in May. The short rains begin in early October, reach a maximum on November, and decline in December. Precipitation rates in the LATE20C simulation follow a very similar pattern. In comparison with coupled GCM simulations, for example, the LATE20 simulation does not underestimate rainfall during the long rains, and the overestimation of rainfall rates during the short rains much less than in the coupled GCMs.

When the averaging area is extended farther north, to 10°N, a shortcoming of the LATE20C simulation is revealed. As shown in Fig. 2b, the ensemble simulation produces excessive rainfall in the boreal summer months over southern Ethiopia. However, even over this larger averaging region, the long-rains and short-rains seasons that are the focus of this paper are well simulated.

Based on the seasonality of precipitation in the observations shown in Fig. 2, we average March, April, and May (MAM) to evaluate the modeled distribution of rainfall during the long rains. Figures 3a-d show seasonal-mean precipitation rates for MAM in the four observational datasets; the LATE20C simulation precipitation climatology is in Fig. 4e. Note that the TMPA and CMORPH datasets do not overlap for the full 20-year period of the LATE20 simulation, so only 11 years are averaged for these datasets. Strongest rainfall rates in the observations fall over western Lake Victoria, eastern Democratic Republic of the Congo (DRC), southeastern/coastal Tanzania, and southern Ethiopia. With the exception of the Lake Victoria precipitation maximum, the model simulation reproduces each of these maxima, but with rainfall rates that are unrealistically high over the DRC. The low precipitation rates

simulated over Lake Victoria occur because lake temperatures in the simulation are prescribed from the NCEP2 reanalysis, where the values are unrealistically low. Despite this local discrepancy, the model simulation produces a reasonable simulation of the observed precipitation maxima and the minima over East Africa.

Based on the observations shown in Fig. 2, we average October, November, and December (OND) to evaluate the modeled distribution of rainfall during the short rains. Figures 4f - j display observed and modeled precipitation rates for OND. Note that some authors use the traditional boreal fall mean (September-October-November) to define the short rains, but the observations presented in Fig. 2 indicate that the rainy season does not start in the equatorial averaging region until early October. During the short rains, the precipitation maxima over Lake Victoria and the eastern DRC are similar to those during the long rains. Similar to MAM, the simulation captures the maximum over the DRC with excessive rainfall rates, but does not produce high rainfall rates over Lake Victoria.

Since a primary analysis tool used here to understand simulated changes in East African precipitation is a decomposition of the atmospheric column moisture budget (section 3.3), the modeled moisture budget is compared with that of the ERA5 reanalysis during the two rainy seasons. This comparison also provides insights into the implications of the too-low prescribed Lake Victoria temperatures and precipitation rates for the larger-scale moisture advection and convergence properties that are the focus of this study.

Figures 5a and b show MAM precipitation and evaporation rates as simulated in the model ensemble mean, respectively, and Figs. 5c-e are the vertically-integrated atmospheric components of the convergence (C, Eq. 3), advection (A, Eq. 4), and residual (R) terms from the vertically-integrated atmospheric column moisture budget (Eq. 2). Figures 5f-j are the same quantities from the ERA5 reanalysis. Note that while precipitation values from reanalyses are not as reliable as the observations shown in Fig. 4 because they depend on parameterizations,

ERA5 (Fig. 5f) reproduces the precipitation maxima observed (Figs. 4a–d). In both the model simulation and reanalysis, evaporation rates largely reflect precipitation (and soil moisture) distributions over land, but with smaller magnitudes. Over Lake Victoria, both precipitation and evaporation rates are unrealistically low in the simulation in association with cool lake surface temperatures.

The atmospheric components of the column moisture budget terms in the simulation (Figs. 5d-e) are similar to those of the ERA5 reanalysis (Fig. 5h-j). In both products C is positive to the east of about 35°E and negative to the west (Figs. 5c and h), and the similarity holds for the meridional and zonal components of C (not shown). R values (Figs. 5e and j) are largely opposite in sign with similar magnitudes compared with C, reflecting the important role of orography in organizing regional rainfall over East Africa. The advection term, A, is generally small (Figs. 5d and i), largely due to compensation between the zonal and meridional components (not shown).

An evaluation of the vertically-integrated moisture budget for the short rains season (OND) also demonstrates good agreement between the modeled and reanalyzed moisture budgets, as shown in Figure 6. These results are similar to those of Liu et al. (2020) who found excellent agreement with the ERA-Interim reanalysis in regional model simulations of the short rains over East Africa.

This comparison between the model and reanalysis builds confidence in the model's ability to correctly represent the large-scale physical processes that underlie the region's precipitation distributions. The comparison also shows that the discrepancies over Lake Victoria – evident especially in the P, E, and C evaluations – are confined to the immediate region of the lake and do not compromise the regional-scale moisture budget analysis.

# 4.2 Simulated changes in East African rainfall

Figure 6 displays differences in precipitation rates averaged over East Africa (land points only; 30-50°E, 10S -10°N) through the annual cycle for the MID21 - LATE20 (green) and LATE21C – LATE20C (red) ensemble means. Solid lines are for the 30-km domain ensemble means (20 members for LATE20 and MID21, 9 members for LATE21), and dashed lines are for the 90-km domain ensemble means (20 members for all three simulations).

Differences between MID21C and LATE21C are small (less than about 0.5 mm/day) in February through September. In mid-October, a positive precipitation anomaly grows to greater than 1 mm/day in early December, and then steeply declines through the rest of the month. The two 20-members ensembles from the 30-km and 90-km model domains produce very similar results.

The intensification of the short rains is repeated in the LATE21 simulation, but with greatly amplified magnitude. The amplitude of this anomaly is smaller in the 20-member ensemble on the 90-km domain than in the 9-member ensemble on the 30-km domain, but in both cases the anomaly exceeds 2.5 m/day in November. In addition, a much smaller positive precipitation anomaly develops in boreal spring, sustained between 0.5 and 1 mm/day in the 30-km ensemble mean but barely at 0.5 mm/day in the 90-km ensemble mean in late March and April.

We conclude that there is a robust and progressive enhancement in the short rains in these simulations. By mid-century, the short rainy season is producing similar precipitation rates to those in the long rains over East Africa in the model simulations, and by the end of the century the short rains surpass the spring rainy season. In the MID21 simulation in boreal spring, precipitation changes are small (< 0.5 mm/day). Rainfall increases occur on the higher-resolution grid in spring, but with only 9 ensemble members and disagreement from the 20-

member ensemble on the coarser grid, we cannot conclude that a signal is emerging by the end of the century.

The emerging greenhouse gas-forced climate change signal provides a limited but real potential opportunity to evaluate climate change simulations. Such a check against observations may not always be conclusive and attributive, especially for precipitation because of its high natural variability and the shortage (and shortness) of observational records, but a comparison with observed change can help build confidence in simulation. Here we note that the simulated differences in precipitation for the mid- and late-21<sup>st</sup> c. are consistent with trends analyzed from observations as reviewed in section 2. These studies uniformly suggest that a wetting signal in the short rains is emerging over East Africa, similar to the projections discussed here and in Cook and Vizy (2013), while results for the long rains are uncertain.

The purpose of this paper is to explain this difference in behavior in the long and short rainy seasons. We begin by investigating the reasons for the enhancement of the short rains, and then compare with the long rains to understand the reasons for the differences in the rainfall response to increasing greenhouse gases. We choose the months of November and April for this analysis since they capture the peak responses in the model, and verify that adjacent months are similar. Averaging over several months to form a seasonal average can distort the dynamical responses, especially during transitional seasons.

# 4.3 Analysis of Short Rains Projections

Differences in the components of the vertically-integrated atmospheric moisture budget for MID21-LATE20 are shown in Figures 7a-h in November across the equatorial East Africa analysis domain. Positive precipitation anomalies (Fig. 7a) are widespread within about 8° of the equator in both hemispheres, with the highest values and statistical significance along the DRC's border with Uganda, Rwanda, and Burundi, and over western Tanzania and eastern

Kenya. While evapotranspiration anomalies are generally positive and statistically significant (Fig. 7b), they do not reflect the structure of the precipitation anomalies. These structures are more prominently reflected in the vertically-integrated moisture convergence term, which is equal to P-E (Eq. 1), shown in Fig. 7c.

The advection term, A (Eq. 3), also produces statistically-significant differences, but with smaller magnitudes and scattered structure. In contrast, the total moisture convergence term, C (Eq. 2; Fig. 7d), reflects the positive precipitation anomalies over Uganda, Rwanda, Burundi, southern South Sudan, and the western DRC as well as western Tanzania. The wetting signal over eastern Kenya is more weakly represented.

The constituents of C,  $C_Z$  (Eq. 5) and  $C_M$  (Eq. 6), are shown in Figs. 7e and f, respectively. In general,  $C_Z$  has its largest and most significant positive values to the west of about 33°N, with significant negative values over much of Kenya.  $C_M$  opposes and overwhelms this zonal moisture divergence over Kenya, and weakens the zonal moisture convergence over South Sudan. The residual term, R (Fig. 7g), produces anomalies that are disorganized and not strongly significant. It supports  $C_M$  in producing positive anomalies over Kenya (along with evapotranspiration), but opposes  $C_M$ 's negative anomalies over southeastern Tanzania.

Comparing the moisture budget decomposition for the LATE21 simulation with that of the MID21 simulation provides an opportunity to clarify and reinforce the conclusions from the MID21 analysis. When an anomaly identified in the MID21 simulation is stronger and/or more widespread in the LATE21 simulation, confidence is enhanced that this anomaly is forced by increasing greenhouse gases (either directly or indirectly through the imposed SSTAs), even if the anomaly is not statistically significant in the MID21 case. However, it is always important to remember that the response to increasing greenhouse gas levels is not necessarily linear.

LATE21-LATE20 anomalies for the components of the vertically-integrated moisture budget are shown in Figs. 7i – p; the 9-member ensemble at 30-km resolution is used. Positive

precipitation anomalies are stronger, more widespread, and of higher statistical significance compared with the MID21 simulation (compare Figs. 7a and i). The similarity in sign and structure of these anomalies adds confidence to the projection of an intensification of the short rains by mid-century.

Each of the components of the vertically-integrated atmospheric moisture budget has anomalies that are similar in structure, but larger significance and magnitudes, to the anomalies for MID21. This indicates that the physical processes responsible for the precipitation at midcentury are the same for the late-21<sup>st</sup>-century.

In summary, both at mid-century and the end of the century, increases in the short rains are primarily associated with differences in the atmospheric hydrodynamics, enhanced but not caused by the increases in evaporation that accompany surface warming. The convergence term (Eq. 2) produces nearly all of the anomaly. The zonal and meridional convergence terms,  $C_Z$  (Eq. 5) and  $C_M$  (Eq. 6), are of opposite sign over much of Kenya but the largely-positive  $C_M$  dominates.  $C_Z$  and  $C_M$  are both positive and contribute to rainfall increases over Tanzania, except in the southeast corner where  $C_M$  is negative. West and north of Lake Victoria,  $C_Z$  and  $C_M$  have opposite signs, with the larger values of  $C_Z$  producing rainfall increases.

The vertically-integrated components of the column moisture budget and their anomalies are well represented by the low-level fields where the specific humidity, q, is large. Figures 8a and b show climatological specific humidity and moisture flux  $(q^-)$  vectors from the LATE20 simulation at 850 hPa and 925 hPa, respectively. Several important features emerge; the hydrodynamics for this region is complicated. One feature is the northeasterly moisture flux across the Horn of Africa and its westward curvature along the equator at both 850 and 925 hPa. At the lower level, the flux is easterly along the entire coast from 10°S to 5°N. At both levels, the westward turning of this northeasterly moisture flux impinges on the topography and carries moisture through the Turkana Channel (near 5°N and 37°E) to sustain

rainfall over South Sudan (Vizy and Cook 2019). West of about 35°E, the moisture flux is weaker than along the coast. It is northeasterly in the Northern Hemisphere, northwesterly in the Southern Hemisphere, and small along the equator.

Differences in specific humidity and moisture fluxes at 850 hPa and 925 hPa for MID21-LATE20 are shown in Figs. 8c and d. The northeasterly moisture flux across Somalia and eastern Ethiopia seen in the full field (Fig. 8a) is about 10% stronger in the MID21 simulation at 850 hPa, but not at 925 hPa. Moisture transport through the Turkana Channel is enhanced at both levels, primarily in association with enhanced onshore flow in the Southern Hemisphere. The curvature of this flow from southerly to easterly over Kenya explains the partial compensation between  $C_Z$  and  $C_M$  in this region (Figs. 7f and g). Zonal moisture convergence north of Lake Victoria occurs when the enhanced southeasterly flux through the Turkana channel converges with an enhanced southwesterly flux over the northeastern DRC and South Sudan.

West of about 35°E, the moisture flux anomalies are easterly along the equator at both levels. They bifurcate around the topography generating the southeasterly anomalies to the north, and northeasterly anomalies to the south. The easterly anomalies along the equator impinge on the topography to enhance zonal moisture convergence and precipitation to the west of Lake Victoria.

As seen in Figs. 8e and f, specific humidity and moisture flux anomalies at 850 hPa and 925 hPa in the LATE21-LATE20 differences have a similar structure, with larger magnitudes, to the MID21-LATE20 differences (Figs. 8c and d). Even more apparent at late century is that there is little enhancement of the northeasterly moisture flux across the Horn of Africa, despite the prominence of this flux in the climatological moisture budget (Figs. 8a and b).

To understand the dynamics of the regional moisture flux anomalies and their relationship to the greenhouse gas forcing factors, we examine geopotential height and wind

fields on a larger space scale. Figures 9a and b display 850-hPa and 925-hPa horizontal wind vectors and geopotential heights for November in the LATE20 ensemble mean. High geopotential heights cover the Sahara and Arabian Deserts, characteristic of the boreal winter climatology. In the Southern Hemisphere, the continental thermal low – the Angola low - is centered near 15°S and 20°E with relatively low geopotential heights extending northward to about 5°N. South of about 20°S, the continent is flanked by subtropical highs over the South Atlantic and South Indian Ocean.

Despite the fact that the East African short rains are often described as occurring during the boreal fall, the season does not begin until October and extends through December (Fig. 2). Most importantly, the large-scale environment in November – the height of the short rains season - is in a characteristic solstitial pattern with summer in the Southern Hemisphere and winter in the Northern Hemisphere (see the geopotential height configuration shown in Figs. 9a and b). One exception is the northward extension of low geopotential heights from the Angola low to the equator – the presence of low geopotential heights centered on the equator is typical of an equinoctial pattern. As seen in Fig. 2, the short rains are at a maximum more than a month after the autumnal equinox, and rainfall does not even begin to increase until after the equinox on or about 21 September. In contrast, the long rains are near their maximum on the date of the vernal equinox (approximately 20 March).

Figures 9a and b indicate that the climatological northeasterly moisture flux across the Horn of Africa seen in Figs. 8a and b is due to the approximately geostrophic flow between high geopotential heights to the northwest over the Sahara and Arabian Peninsula, and low geopotential heights to the southeast over the equatorial western Indian Ocean. Within about 5° of the equator, with small Coriolis accelerations, the flow curves westward down the geopotential height gradient.

Farther south along the east coast, anticyclonic flow about the South Indian subtropical high (the Mascarene high) meets the cyclonic flow about the Angola low. This interaction is typical of the land-based convergence zones that develop in the Southern Hemisphere in summer, in particular the South Indian convergence zone (SICZ; Cook 2000, Lazenby et al. 2015).

Differences in winds and normalized geopotential heights at 850- and 925-hPa are shown in Figs. 9c and d, respectively, for MID21-LATE20. Normalized geopotential heights are calculated by subtracting the domain-averaged geopotential height anomaly from the local anomaly. Since geopotential heights increase throughout the domain in the future simulations, normalizing clarifies the relative changes in geopotential heights that are associated with the wind anomalies.

At 850 hPa and 925 hPa, the summer hemisphere thermal low and the Mascarene high are both stronger in the mid-century simulation. In addition to strengthening, the Mascarene high moves poleward and westward; the largest positive anomalies are near 20°S in the MID21 simulation while the center of the high is at 33°S in the LATE20 simulation. North of about 5°S, normalized geopotential height are lower in the Indian Ocean equatorial trough. These differences in the equatorial trough and Mascarene high increase the negative meridional geopotential height gradients in the western Indian Ocean between 15°S and 5°S, and increase the onshore – largely geostrophic - flow and moisture flux across the East Africa coast. This mechanism for climate change is consistent with observations of climate variability, since the position and strength of the Mascarene High has been observed to affect the timing and intensity of the East African short rains (Manatsa et al. 2016).

The enhanced moisture flux through the Turkana Channel and the southwesterly moisture flux anomalies that lead to precipitation increases north of Lake Victoria are both related to negative geopotential height anomalies over the eastern Sahara. These anomalies

represent a weakening of the wintertime high geopotential heights over the land surface. The zonal moisture flux and convergence anomalies that support precipitation increases west of Lake Victoria are associated with westerly flow anomalies along the equator that are associated with the negative geopotential height anomalies over the eastern Sahara and, to a lesser extent, southern Africa.

Note that even though the northeasterly flow over the Horn of Africa is weaker in the MID21 simulation, as indicated by the southwesterly wind anomalies in Figs. 9c and d, increases in specific humidity compensate for the weaker winds so the moisture flux differences in this region are small (Figs. 9c and d).

The same patterns in normalized geopotential height and moisture flux anomalies occur in the LATE21-LATE20 differences (Figs. 9e and f), but with larger magnitudes that support the larger precipitation enhancements projected for the end of the century (Fig. 8).

In summary, for both the mid- and late-century simulations, enhancements in the short rains are primarily associated with differences in the vertically-integrated moisture convergence. Decomposing the vertically-integrated moisture convergence shows that the differences are related to low-level circulation anomalies that are associated with a strengthening of the Southern Hemisphere (the summer hemisphere) thermal low/subtropical high pattern and a weakening of high geopotential heights over the eastern Sahara. The final step is to relate these influential geopotential height anomalies to the climate forcing factors. In the simulations, these are the direct effects of increasing atmospheric CO<sub>2</sub> and the indirect effects of increasing atmospheric CO<sub>2</sub> due to the imposed SSTAs.

Figures 10a and b display November surface temperature anomalies for the MID21-LATE21 and LATE21-LATE20 simulations, respectively. For the MID21 simulation, SSTAs are 1-2 K in the eastern Atlantic and western Indian Ocean. They are 2 – 3.5 K in the LATE21 simulation. Warming anomalies are fairly uniform across land and ocean surfaces deep in the

tropics, within about 6° of the equator, while subtropical latitudes feature land surface warming anomalies that are 2 or 3 times greater than the SSTAs at the same latitude. Two exceptions, however are SSTAs in the Red Sea and Persian Gulf. North of 15°N, Red Sea temperature increases are similar to those of the surrounding land surfaces. While these SSTAs are prescribed from an average of CGCM simulations as described in section 3, recent observations of warming trends suggest that these elevated SSTAs are reasonable. For example, Chaidez et al. (2017) estimate that the Red Sea is warming at a rate of 0.17 K/decade on average, with amplified warming rates of 0.30-0.45 K/decade the north of 23°N. In comparison, the warming rate for the global oceans is estimated at 0.11 K/decade. Consistent with amplified warming over the Red Sea, temperature increases in the eastern Sahara are higher than those in the central and western Sahara. The result is a shift of atmospheric mass to the west and positive geopotential height anomalies over the eastern Sahara.

In the Southern Hemisphere subtropics, the enhanced intensity of the Angola low and the Mascarene high occur because land surface temperatures (which are calculated in the land surface model as a response to the surface heat balance) increase more than SSTs south of about 8°S. This warming pattern shifts mass from the vertical column over southern Africa to intensify both the thermal Angola low and the Mascarene high. This result is physically meaningful and expected due to the lower heat capacity of the relatively dry subtropical land surface compared with the ocean. The South Atlantic subtropical high does not intensify. Rather, it is observed to be shifting eastward in response to SSTAs in the western South Atlantic and an adjustment of the South Atlantic convergence zone (Vizy et al. 2018).

# 4.3 Analysis of Longs Rains Projections

The April monthly mean is used to evaluate differences in the long rains season as greenhouse gases increase. Figures 11a-h show differences in the components of the vertically-

integrated atmospheric moisture budget for MID21-LATE21. Consistent with Fig. 6, and in contrast with the November case (Fig. 7a), significant precipitation differences are not simulated for mid-century. Evapotranspiration anomalies (Fig. 11b) are widespread and significant in some regions, consistent with surface warming. Differences in P-E are small (Fig. 11c) but similar to the precipitation anomalies, and advection term anomalies are small (Fig. 11d). While some significance emerges in the convergence term differences (Fig. 11e), there are no coherent patterns. As seen in Figs. 11f and g,  $C_z$  and  $C_m$  anomalies exhibit larger-scale coherence, but they are largely in opposition. The residual, R in Fig. 11h, produces scattered regions of significance that are opposite in sign to C (Fig. 11e).

At the end of the 21<sup>st</sup> century, increases in precipitation are widespread over Kenya and most of Tanzania, but very little statistical significance emerges (Fig. 11i). The other components of the moisture budget anomalies in the LATE21 simulation (Figs. 11j-p) are similar in most respects to the MID21 simulation, but coherent regions of statistical significance do not emerge.

What accounts for the difference in the April and November responses? One possibility is that the surface temperature response is different in the two months. Figures 12a and b show differences in the April surface temperature for MID21-LATE20 and LATE21-LATE20, respectively. The surface temperature differences are quite similar in April and November (compare with Fig. 10). The most notable differences include a slightly warmer central equatorial Africa in April and, for the LATE21 differences, smaller temperature differences over southern Africa and the Red Sea region.

The more important difference between November and April is the background (basic state) circulation. Figures 13a and b show geopotential heights and wind vectors from the control climatology (LATE20) for April at 850 hPa and 925 hPa, respectively. This is an equinoctial pattern and not a solstitial pattern as occurs in November (Figs. 9a and b). The

thermal low is centered near the equator, and the Mascarene high extends farther west and onto the continent in the absence of the Angola low. High geopotential heights over northern Africa are weaker than in November as the region transitions to the summer pattern with a thermal low in place over the Sahara and Arabian Deserts. In particular, the circulation features that were perturbed by the CO<sub>2</sub>-related forcing to cause November precipitation increases in equatorial East Africa are absent in the April base state (LATE20). There is no Angola low present to strengthen and interact with a stronger Mascarene high, and no flow from the west along the equator.

Circulation and normalized geopotential height anomalies for April in the MID21 case (Figs. 13c and d) are small across the tropics. There is weak large-scale wind and moisture (not shown) divergence from 10°S to the equator associated with anomalous easterlies to the west and anomalous westerlies to the east, but the associated moisture flux divergence is compensated for by an anomalous southerly flux of moisture associated with an advanced formation of the zonal branch of the Somali jet.

While the circulation and geopotential height anomalies for the MID21 and LATE21 are similar in November (Figs. 9c-f), differing only in magnitude, the same is not true for April. Warming in the subtropics of both hemispheres becomes large enough in the LATE21 simulation to produce anomalous lows in the normalized geopotential height fields. In the Southern Hemisphere, the LATE21 April anomalies resemble those for November for both the MID21 and LATE21 cases. However, the associated wind and moisture flux (not shown) anomalies are small and superimposed on a very different base state, and they do not lead to precipitation enhancements.

### 5. Summary and Conclusions

Ensemble simulations of the late 20<sup>th</sup> century (1989 to 2008), mid-21<sup>st</sup> century (2041-2060), and late 21<sup>st</sup> century (2081-2100) climate over equatorial East Africa at 30-km resolution are analyzed. Future simulations are created by increasing atmospheric CO<sub>2</sub> levels in a regional model according to the RCP8.5 emissions scenario, and adding anomalies to observed SSTs and lateral boundary conditions derived from coupled GCM (CMIP5) simulations. The control simulation produces an accurate simulation of observed East African precipitation and atmospheric hydrodynamics of the late 20<sup>th</sup> century, including rainfall amounts and their seasonality. This improvement over CGCM simulations, which generally fail to capture the long rains and over-produce short rains, is attributable to the selection of physical parameterizations to optimize the regional simulation, the improved accuracy of SST distributions, and the higher horizontal resolution that provides a more accurate representation of the region's complex and influential topography, including the Turkana Channel. Of particular relevance for the East African climate is a more accurate depiction of the complex and influential topography, including the Turkana Channel.

The twenty-first century rainfall projections over equatorial East Africa indicate that rainfall will increase during the short rains season (October through December) but not during the long rains season (March through May). These projections are consistent with current observations. The purpose of this paper is to understand the reason for the seasonal asymmetry in the response.

In the model simulations for November, representing the short rains, rainfall rates increase by approximately 30% over a large portion of equatorial East Africa (10S-10°N; 30°E-50°E) by the mid-21<sup>st</sup> century, and by about 100% by the end of the century. An analysis of the atmospheric column moisture budget attributes these increases to differences in the low-level wind convergence in a moist environment rather than changes in evapotranspiration or

moisture gradients. Amplified warming over summer hemisphere land compared with the adjacent oceans amplifies the Angola low and the Mascarene high, increasing the onshore easterly flow and moisture flux across the East Africa coast. Rainfall is enhanced when the anomalous flow impinges on the East African topography, and the moisture flux through the Turkana Channel is also strongly enhanced. The southeasterly flux through the Turkana Channel converges with westerly anomalies that are associated with a weakening of high geopotential heights over the eastern Sahara to support precipitation increases west of 35°E. Amplified SSTAs in the Red Sea are associated with temperature increases in the eastern Sahara that are higher than those in the central and western Sahara, shifting atmospheric mass to the west and leading to the weakening of high geopotential heights over the eastern Sahara. This thermal response to increasing atmospheric greenhouse gases is physically meaningful and expected due to the lower heat capacity of the relatively dry subtropical land surface compared with the ocean, lending confidence to the precipitation projections.

The long rains are not amplified at all in the mid-21<sup>st</sup> c. simulation, and they are only slightly stronger in the late-21st c. simulation. This is consistent with recent research which shows that a low period in the long rains from approximately 1998-2009 may not represent a greenhouse gas-forced trend in long-rains precipitation rates (see Fig. 1a in Wainwright et al 2019 and Fig. 4 in Cook and Vizy 2019), and also with studies of variability on intraseasonal to interannual time scales that find the long rains are less sensitive to remote SST forcing than the short rains (e.g., Ogallo et al. 1988; Mutai and Ward 2000; Dutra et al 2013; Nicholson 2014; MacLeod 2019).

The fundamental reason for the seasonal asymmetry in the response to increased atmospheric CO<sub>2</sub> over equatorial East Africa, with strongly enhanced short rains and little response in the long rains, is the background state that is perturbed by greenhouse-gas forcing. While the East African short rains are usually described as occurring during the boreal fall, the

maximum is in late fall, or even early winter (Fig. 2). During November, which is the short-rains maximum, the climatological basic state is a characteristic solstitial pattern with summer in the Southern Hemisphere and winter in the Northern Hemisphere (Figs. 9a and b). The short rains are at a maximum more than one month after the autumnal equinox, and rainfall does not even begin to increase until after the equinox on or about 21 September. In contrast, the long rains are already near their maximum on the date of the vernal equinox (approximately 20 March), and the background state is an equinoctial pattern with a continental thermal low centered near the equator (Figs. 13a and b). Unlike the November case, this equinoctial pattern deep in the tropics is not connected with or strongly perturbed by changes in the subtropical atmospheric hydrodynamics.

With a basic state climate that validates well, producing accurate simulations of both of East Africa's rainy seasons as well as the regional circulation systems, these simulations and projections represent an improvement over GCM simulations. One reason is that the 30-km resolution used here allows for a more accurate representation of the region's important topography, including the Turkana channel which is crucial for the hydrodynamical response to CO<sub>2</sub> increases. Another reason for the improvement compared with GCMs is the choice of physical parameterizations that work well over Africa. Without these improvements in modeling the climate of East Africa, the analysis of the asymmetrical response to greenhouse gas-forcing would not be as reliable.

In addition to the relative accuracy of the simulated late 20<sup>th</sup> c. climate, further confidence in the results derives from the ensemble simulation design which allows for the calculation of statistical significance. The emerging greenhouse gas-forced climate change signal has also been used to provide verification, albeit limited at this time by the combination of natural variability and observational constraints. Finally, delving into the dynamics of the precipitation response, relating the simulated differences in rainfall to changes in atmospheric

circulation and moisture and, finally, to the direct and indirect forcing factors (atmospheric CO2 increases and SSTAs, respectively) builds further confidence in the projections. Confidence in projections is a crucial issue because the simulated changes in the short rains are quite large and will require infrastructural adaptation to avoid the severe socioeconomic consequences that accompany flooding, crop spoilage, and soil nutrient run off.

# Acknowledgements

Support from NSF Award #1701520 is gratefully acknowledged. The HPC and database resources needed for the simulations and analysis were supplied by the Texas Advanced Computing Center (TACC) at The University of Texas at Austin. URL: http://www.tacc.utexas.edu.

698	References
699	
700	Ashouri H, Hsu K-L, Sorooshian S, Braithwaite DK (2015) PERSIANN-CDR: Daily
701	precipitation climate data record from multi-satellite observations for hydrological
702	and climate studies. Bull. Amer. Meteor. Soc., 96: 69-
703	83. https://doi.org/10.1175/BAMS-D-13-00068.1
704	Bahaga TK, Tsido GM, Kucharski F, Diro GT (2015) Potential predictability of the sea-
705	surface temperature forced East African short rains interannual variability in the $20^{\text{th}}$
706	century. Quart. J. Roy. Meteorol. Soc. 141: 16-26.
707	Bahaga TK, Fink AH, Knippertz P (2019) Revisiting interannual to decadal teleconnections
708	influencing seasonal rainfall in the Greater Horn of Africa during the 20th century. Int
709	J. Climatology 39: 2765-2785.
710	Behera SK, Luo JJ, Masson S et al. (2005) Paramount impact of the Indian Ocean dipole on
711	the East African short rains: A CGCM study. J. Climate 18:4514-4530
712	Black E, Slingo J, Sperber KR (2003) An observational study of the relationship between
713	excessively strong short rains in coastal East Africa and Indian Ocean SST. Mon
714	Weather Rev, 131, 74-94.
715	Busby JW, Cook KH, Vizy EK, Smith TG, Bekalo M (2014) Identifying hot spots of security
716	vulnerability associated with climate change in Africa. Climatic Change, 124: 717-
717	731.
718	Cattani E, Merino A, Guijarro JA, Levizzani V (2018) East Africa rainfall trends and
719	variability 1983-2015 using three long-term satellite products. Remote Sensing
720	10(6), 931, https://doi.org/10.3390/rs10060931

721 Chaidez V, Dreano, Agusti S, Duarte CM, Hoteit I (2017) Decadal trends in Red Sea 722 maximum surface temperature. Scientific Reports, 7:8144, DOI:10.1038/s41598-017-08146-z 723 724 Chen, S-H, Sun Y-W (2002) A one-dimensional time dependent cloud model. J. Meteor. Soc. Japan, 80: 99-118. 725 Chen F, Dudhia J (2001) Coupling an advanced land surface–hydrology model with the Penn 726 State-NCAR MM5 modeling system. Part I: Model description and implementation. 727 Mon. Wea. Rev., 129: 569-585. 728 729 Cook KH (2000) The South Indian Convergence Zone and interannual rainfall variability over southern Africa. J. Climate, 13: 3789-3804. 730 Cook KH, Vizy EK (2006) South American climate during the Last Glacial Maximum: 731 732 Delayed onset of the South American monsoon. J. Geophy. Res. – Atmospheres, 111, D02110, doi:10.1029/2005JD005980. 733 Cook KH, Vizy EK (2012) Impact of climate change on mid-21st century growing seasons in 734 735 Africa. Climate Dynamics: 39, 2937-2955. Cook KH, Vizy EK (2013) Projected changes in East African rainy seasons. J Climate 26: 736 737 5931-5948. https://doi.org/10.1175/JCLI-D-12-00455.1 Cook KH, Vizy EK (2019) Contemporary climate change of the African monsoon systems. 738 Current Climate Change Reports 5:145-159. https://doi.org/10.1007/s40641-019-739 740 00130-1 Dunning CM, Allan RP, Black E (2017) Identification of deficiencies in seasonal rainfall 741 simulated by CMIP5 climate models. Environmental Research Lett. 12: Art. No. 742 114001 743 Dutra E, Magnusson L, Wetterhall F, Cloke HL, Balsamo G, Boussetta S, Pappenberger F 744

(2013) The 2010–2011 drought in the Horn of Africa in ECMWF reanalysis and

745

746 seasonal forecast products. Int J Climatol 33(7):1720–1729. https://doi.org/10.1002/joc.3545 747 Endris HS, Omondi P, Jain S, Lennard C, Hewitson B, Chang'a L, Awange JL, Dosio A, 748 749 Ketiem P, Nilulin G, and co-authors (2013) Assessment of the performance of CORDEX regional climate models in simulating East African rainfall. J. Climate 26: 750 8453-8475. 751 ERA5 (2018) Generated using Copernicus Climate Change Service Information 2018. 752 http://apps.ecmwf.int/data-catalogues/era5/?class=ea 753 754 Finney DL, Marsham JH, Jackson LS, Kendon EJ, Rowell DP, Boorman PM, Keane RJ, Stratton RA, Senior CA (2019) Implications of improved representation of convection 755 for the East Africa water budget using a convective-permitting model. J Climate, 32: 756 757 2109-2129. https://doi.org/10.1175/JCLI-D-18-0387.1 Funk C, Hoell A, Husak G, Shukla S, Michaelsen J (2015) The East African monsoon 758 system: seasonal climatologies and recent variations. Chapter for "The Monsoons and 759 Climate Change", Leila M. V. Carvalho and Charles Jones (Eds.). 760 https://doi.org/10.1007/978-3-319- 21650-8 1 761 Funk C, Peterson P, Landsfeld M, Pedreros D, Verdin J, Shukla S, Husak G, Rowland J, 762 Harrison L, Hoell A, Michaelsen J (2015) The climate hazards infrared precipitation 763 with stations – a new environmental record for monitoring extremes. Scientific Data 2: 764 765 150066. https://doi.org/10.1038/sdata.2015.66 Gebrechorkos SH, Hülsmann S, Bernhofer C (2019) Long-term trends in rainfall and 766 temperature using high-resolution climate datasets in East Africa. Sci Rep 9: 11376. 767 https://doi.org/10.1038/s41598-019-47933-8 768

769 Han F, Cook KH, Vizy EK (2019) Changes in intense rainfall events and drought across 770 Africa in the 21st century. Clim. Dyn. 53: 2757-2777. https://doi.org/10.1007/s00382-019-04653-z 771 772 Hartman AT (2018) An analysis of the effects of temperatures and circulations on the strength of the low-level jet in the Turkana Channel in East Africa. Theor Appl 773 Climatol 132:1003–1017. https://doi.org/10.1007/s0070 4-017-2121-x 774 Hong S-Y, Noh Y, Dudhia J (2006) A new vertical diffusion package with an explicit 775 treatment of entrainment processes. Mon. Wea. Rev: 134, 2318–2341. 776 777 Huffman GJ, Adler RF, Bolvin DT, Gu G, Nelkin EJ, Bowman KP, Hong Y, Stocker EF, Wolff DB (2007) The TRMM multisatellite precipitation analysis (TMPA): quasi-778 global, multiyear, combined-sensor precipitation estimates at fine scales. J 779 780 Hydrometeorol 8:38–55. https://doi.org/10.1175/JHM560.1 781 Joyce R, Janowiak J, Arkin PA, Xie P (2004) CMORPH: A method that produces global precipitation estimates from passive microwave and infrared data at high spatial and 782 temporal resolution. J Hydrometeor 5: 487-503. https://doi.org/10.1175/1525-783 7541(2004)005<0487:CAMTPG>2.0.CO;2 784 785 Kain, JS (2004) The Kain–Fritsch convective parameterization: An update. J. Appl. Meteor: 43, 170–181. 786 Kilavi M, MacLeod D, Ambani M, Robbins J, Dankers R, Graham R, Helen T, Salih AAM, 787 788 Todd MC (2018) Extreme rainfall and fooding over central Kenya including Nairobi city during the long-rains season 2018: causes, predictability, and potential for early 789 warning and actions. Atmosphere 9(12):472 790 791 Kanamitsu M, Ebisuzaki W, Woollen J, Yang SK, Hnilo JJ, Fiorino M, Potter GL (2002)

NCEP-DOE AMIP-II Reanalysis (R2). Bull. Amer. Meteor. Soc: 83, 1631-1643.

792

793	Lazenby MJ, Todd MC, Wang Y (2015) Climate model simulation of the South Indian Ocean
794	Convergence Zone: Mean state and variability. Climate Research 68: 1
795	https://doi.org/10.3354/cr01382
796	Lenters JD, Cook KH (1995) Simulation and diagnosis of the regional South American
797	precipitation climatology. J. Climate, 8: 2988-3005.
798	Liebmann B, Hoerling MP, Funk C, Bladé I, Dole RM, Allured D, Quan X, Pegion P,
799	Eischeid JK (2014) Understanding recent Horn of Africa rainfall variability and
800	change. J Climate 27: 8629-8645. https://doi.org/10.1175/JCLI-D-13-00714.1
801	Liebmann B, Blade I, Funk C, Allured A, Quan XW, Hoerling M, Hoell A, Peterson P,
802	Thiaw WM (2017) Climatology and interannual variability of boreal spring wet
803	season precipitation in the eastern Horn of Africa and implications for its recent
804	decline. J. Climate 30: 3867-3886. https://doi.org/ 10.1175/JCLI-D-16-0452.1
805	Liu WR, Cook KH, Vizy EK (2020) Influence of Indian Ocean SST regionality on the East
806	African Short Rains. Accepted for Climate Dynamics.
807	Lu B, Ren HL, Scaife AA, Wu J, Dunstone N, Smith D, Wan JH, Eade R, MacLachlan C,
808	Gordon M (2016) An extreme negative Indian Ocean Dipole event in 2016: dynamics
809	and predictability. Climate Dynamics, 51, 89-100.
810	Lyon B, DeWitt DG (2012) A recent and abrupt decline in East African long rains. Geophys
811	Res Lett 39: L02702. https://doi.org/10.1029/2011GL050337
812	MacLeod D (2019) Seasonal forecasts of the East African long rains: Insight from
813	atmospheric relaxation experiments. Climate Dynamics, 53, 4505-4520.
814	https://doi.org/10.1007/s00382-019-04800-6
815	Maidment RI, Allan RP, Black E (2015) Recent observed and simulated changes in
816	precipitation over Africa. Geophys Res Lett 42: 8155-8164.
817	https://doi.org/10.1002/2015GL065765

818	Manatsa D, Mudavanhu C, Mushore TD, Mavhura E (2016) Linking major shifts in East
819	African short rains to the Southern Annual Mode. Int. J. Climatology 36:1590-1599.
820	Mlawer EJ, Taubman SJ, Brown PD, Iacono MJ, Clough South America (1997) Radiative
821	transfer for inhomogeneous atmosphere: RRTM, a validated correlated-k model for
822	the longwave. J. Geophys. Res., 102: 16 663–16 682.
823	Mutai CC, Ward MN (2000) East African rainfalland the tropical circulation/convection on
824	intraseasonal tointerannual timescales. J Clim 13(22):3915–3939.
825	https://doi.org/10.1175/1520- 0442(2000)0132.0.CO;2
826	Ndomeni, CW, Cattani E, Merino A, Levizzani V (2018) An observational study of the
827	variability of East African rainfall with respect to sea surface temperature and soil
828	moisture. Quart. J. Royal Meteorol. Soc., 144, 384-404.
829	Nicholson SE (2014) The predictability of rainfall over the Greater Horn of Africa. Part I.
830	Prediction of seasonal rainfall. J. Hydrometeorology, 15, 1011-1027.
831	https://doi.org/10.1175/JHM-D-13-062.1
832	Nicholson SE (2016) The Turkana low-level jet: mean climatology and association with
833	regional aridity. Int. J. Climatology: 36, 2598-2614.
834	Ogallo LJ, Janowiak JE, Halpert MS (1988) Teleconnection between seasonal rainfall over
835	East Africa and global sea surface temperature anomalies. J Meteorol Soc Jpn
836	66(6):807–821. https://doi. org/10.2151/jmsj1965.66.6_807
837	Omondi P, Ogallo LA, Anya R, Muthama JM, Ininda J (2013) Linkages between global sea
838	surface temperatures and decadal rainfall variability over Eastern Africa region. Int. J.
839	Climatology 33:2082-2104.
840	Ongoma V, Chen H (2017) Temporal and spatial variability of temperature and precipitation
841	over East Africa from 1951 to 2010. Meteorol Atmos Phys 129: 131-144.
842	https://doi.org/10.1007/s00703-016-0462-0

843	Ongoma V, Chen HS, Gao CJ (2019) Evaluation of CMIP5 twentieth century rainfall
844	simulation over the equatorial East Africa. Theoretical Applied Climatology 135:
845	893-910. https://doi.org/10.1007/s00704-018-2392-x
846	Otieno VO, Anyah RO (2013) CMIP5 simulated climate conditions of the Greater Horn of
847	Africa (GHA). Part I: Contemporary climate. Climate Dyn 41: 2081–2097.
848	https://doi.org/10.1007/s00382-012-1549-z
849	Patricola CM, Cook KH (2007) Dynamics of the West African Monsoon under mid-
850	Holocene precessional forcing: Regional climate model simulations. J. Climate: 20,
851	694-716.
852	Patricola CM, Cook KH (2011) Sub-Saharan Northern African climate at the end of the 21st
853	century: Forcing factors and climate change processes. Climate Dynamics, 37, 1165-
854	1188.
855	Ritchie J, Dowlatabadi H (2017) The 1000 GtC coal questions: Are cases of vastly expanded
856	future coal combustion still plausible? Energy Economics, 65: 16-31.
857	Rowell DP, Booth BBB, Nicholson SE, Good P (2015) Reconciling past and future rainfall
858	trends over East Africa. J Climate 28: 9768-9788. https://doi.org/10.1175/JCLI-D-15-
859	0140.1
860	Saji NH, Yamagata T (2003) Possible impacts of Indian Ocean dipole mode events on global
861	climate. Climate Res. 25: 151-169.
862	Skamarock WC, Klemp JB, Dudhia J, Gill DO, Duda MG, Huang X-Y, Wang W, Powers JG
863	(2008) A description of the Advanced Research WRF Version 3. NCAR Technical
864	Note, NCAR/TN-475+STR.
865	Ummenhofer CC, Sen Gupta A, England MH, Reason CJC (2009) Contributions of Indian
866	Ocean sea surface temperatures to enhanced East African rainfall. J. Climate 22:993-
867	1013.

868	Ummenhofer CC, Kulüke M, Tierney JE (2018) Extremes in East African hydroclimate and
869	links to Indo-Pacific variability on interannual to decadal timescales. Clim Dyn 50:
870	2971-2991. https://doi.org/10.1007/s00382-017-3786-7
871	Vizy EK, Cook KH (2002) Development and application of a mesoscale climate model for
872	the tropics: Influence of sea surface temperature anomalies on the West African
873	monsoon. J. Geophys. Res Atmos., 107(D3), 10.1029/2001JD000686, 2002.
874	Vizy EK, Cook KH (2012) Mid-21 <sup>st</sup> century changes in extreme events over Northern and
875	Tropical Africa, J. Climate: 25, 5748-5767.
876	Vizy EK, Cook KH, Crétat J, Neupane N (2013) Projections of a wetter Sahel in the 21st
877	century from global and regional models. J. Climate, 26: 4664-4687.
878	Vizy EK, Cook KH, Chimphamba J, McCusker B (2015) Projected changes in Malawi's
879	growing season. Climate Dynamics, 45: 1673-1698.
880	Vizy EK, Cook KH, Sun XM (2018) Decadal changes of the South Atlantic Ocean Angola-
881	Benguela frontal zone since 1980. Climate Dynamics 51: 3251-3273.
882	https://doi.org/10.1007/s00382-018-4077-7
883	Vizy EK, Cook KH (2019) Observed relationship between the Turkana low-level jet and
884	boreal summer convection. Clim. Dyn., 53, 4037 – 4058.
885	https://doi.org/10.1007/s00382-019-04769-2
886	Vizy EK, Cook KH (2020) Interannual variability of East African rainfall: Role of seasonal
887	transitions of the low-level cross-equatorial flow. Clim. Dyn.
888	https://doi.org/10.1007/s00382-020-05244-z
889	Wainwright CM, Marsham JH, Keane RJ et al. (2019) 'Eastern African Paradox' rainfall
890	decline due to shorter not less intense Long Rains. npj Clim Atmos Sci 2, 34 (2019).
891	https://doi.org/10.1038/s41612-019-0091-7

892	Williams AP, Funk C (2011) A westward extension of the warm pool leads to a westward
893	extension of the Walker circulation, drying eastern Africa. Climate Dyn 37: 2417-
894	2435. https://doi.org/10.1007/s00382-010-0984-y
895	Xie P, Joyce R, Wu S, Yoo S-H, Yarosh Y, Sun F, Lin R (2017) Reprocessed, biased-corrected
896	CMORPH global high-resolution precipitation estimates from 1998. J Hydrometeorol
897	18: 1617-1641. https://doi.org/10.1175/JHM-D-16-0168.1
898	Yang WC, Seager R, Cane MA, Lyon B (2014) The East African long rains in observations
899	and models. J Climate 27: 7185-7202. https://doi.org/10.1175/JCLI-D-13-00447.1
900	Yang WC, Seager R, Cane MA, Lyon B (2015) The rainfall annual cycle bias over East
901	Africa in CMIP5 coupled climate models. J Climate 28: 9789-9802.
902	https://doi.org/10.1175/JCLI-D-15-0323.1
903	

904	Figure Captions
905	
906	Figure 1. Nested domains for the regional climate model simulations with topography (m)
907	shaded. The outer domain has 90-km resolution, while the inner domain (purple box) has 30-
808	km resolution.
909	
910	Figure 2. 20-day running mean of precipitation in the LATE20C 30-km simulations (blue)
911	TRMM (green), CHIRPS2 (red), PERSIANN (black), and CMORPH (orange) averaged over
912	(a) 30 to $50^{\circ}E$ and $10S$ to $5^{\circ}N$ and (b) 30 to $50^{\circ}E$ and $10S - 10^{\circ}N$ .
913	
914	Figure 3. MAM precipitation climatologies (mm/day) from (a) TMPA, (b) CMORPH, (c)
915	CHIRPS2, (d) PERSIANN, and (e) LATE20. OND precipitation climatologies (mm/day) from
916	(f) TMPA, (g) CMORPH, (h) CHIRPS2, (i) PERSIANN, and (j) LATE20. Years averaged are
917	indicated for each panel. White regions indicate rainfall rates below 1 mm/day and, in (c) and
918	(d), missing data over the ocean.
919	
920	Figure 4. Moisture budget terms from LATE20C and ERA5 during the long rain months
921	(March – May). Panels (a) – (e) display the moisture budget terms: P –precipitation (a), E –
922	evaporation (b), C - vertically integrated moisture convergence (c), A - vertically integrated
923	moisture advection (d), and $R$ – residual (e), for LATE20C model output. Panels (f) – (j) are
924	the same terms calculated in the ERA5 reanalysis.
925	

Figure 5. As in Fig. 4, but averaged over the short rain months (October – December).

Figure 6. 20-day running mean precipitation differences for MID21C-LATE20C (green) and

928 LATE21C-LATE20C (red) in the 30-km simulations (solid) and 90-km simulations (dashed).

All values are averaged over land points from 30-50°E and 10S-10°N. Units are mm/day.

930

931

932

933

934

935

936

929

927

Figure 7. Differences in (a) precipitation, (b) evapotranspiration, (c) precipitation -

evapotranspiration, (d) moisture advection term, (e) moisture convergence term, (f) zonal

moisture convergence term, (g) meridional moisture convergence term, and (h) residual term

in the moisture budget in November for MID21-LATE20. (i) - (p) are the same as (a) - (h) but

for the LATE21-LATE20 differences. Units are mm/day. Black (purple) stippling denotes

values that are statistically significant at the 90% (95%) confidence level.

937

938

939

940

941

942

943

944

Figure 8. Climatological horizontal moisture flux (vectors; kg m kg-1 s-1) and specific

humidity (g/kg) climatologies in November from the LATE20 simulation at (a) 850 hPa and

(b) 925 hPa. November horizontal moisture flux (vectors; kg m kg-1 s-1) and specific humidity

(g/kg) anomalies for the MID21-LATE20 difference at (c) 850 hPa and (d) 925 hPa. November

horizontal moisture flux (vectors; kg m kg-1 s-1) and specific humidity (g/kg) anomalies for

the LATE21-LATE20 difference at (e) 850 hPa and (f) 925 hPa. Vector scales and color bars

are the same for (a) and (b), for (c) and (d), and for (e) and (f).

945

946

947

948

949

950

951

Figure 9. Climatological horizontal wind (vectors; m/s) and geopotential height (shaded; gpm)

in November from the LATE20 simulation at (a) 850 hPa and (b) 925 hPa. Horizontal wind

differences (vectors; m/s) and normalized geopotential height differences (shaded; gpm) in

November for MID21C-LATE20C at (c) 850 hPa and (d) 925 hPa. Horizontal wind differences

(vectors; m/s) and normalized geopotential height differences (shaded; gpm) in November for

LATE21C-LATE20C at (e) 850 hPa and (f) 925 hPa. Topography is masked in white.

952	
953	Figure 10. November surface temperature differences (K) for the (a) MID21-LATE20 and (b)
954	LATE21-LATE20 ensemble means.
955	
956	Figure 11. Differences in (a) precipitation, (b) evapotranspiration, (c) precipitation -
957	evapotranspiration, (d) moisture advection term, (e) moisture convergence term, (f) zonal
958	moisture convergence term, (g) meridional moisture convergence term, and (h) residual term
959	in the moisture budget in April for MID21-LATE20. (i) - (p) are the same as (a) - (h) but for
960	the LATE21-LATE20 differences. Units are mm/day. Black (purple) stippling denotes values
961	that are statistically significant at the 90% (95%) confidence level.
962	
963	Figure 12. April surface temperature differences (K) for the (a) MID21-LATE20 and (b)
964	LATE21-LATE20 ensemble means.
965	
966	Figure 13. Climatological horizontal wind (vectors; m/s) and geopotential height (shaded; gpm)
967	in April from the LATE20 simulation at (a) 850 hPa and (b) 925 hPa. Horizontal wind
968	differences (vectors; m/s) and normalized geopotential height differences (shaded; gpm) in
969	April for MID21C-LATE20C at (c) 850 hPa and (d) 925 hPa. Horizontal wind differences
970	(vectors; m/s) and normalized geopotential height differences (shaded; gpm) in April for
971	LATE21C-LATE20C at (e) 850 hPa and (f) 925 hPa. Topography is masked in white.
972	
973	
974	
975	

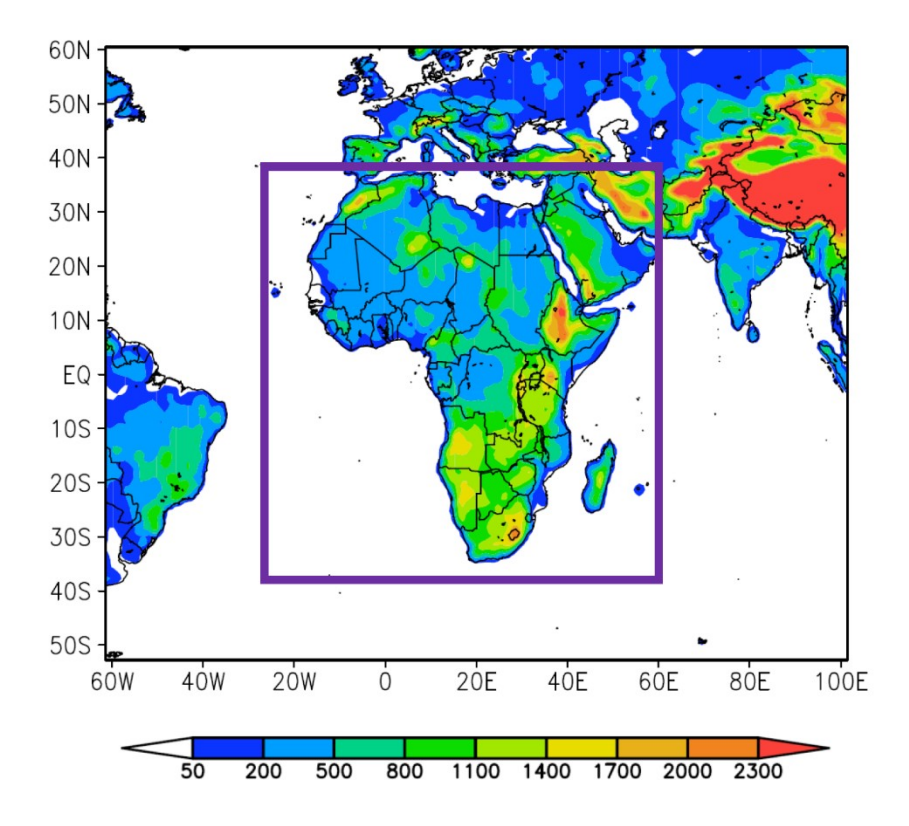


Figure 1. Nested domains for the regional climate model simulations with topography (m) shaded. The outer domain has 90-km resolution, while the inner domain (purple box) has 30-

km resolution.

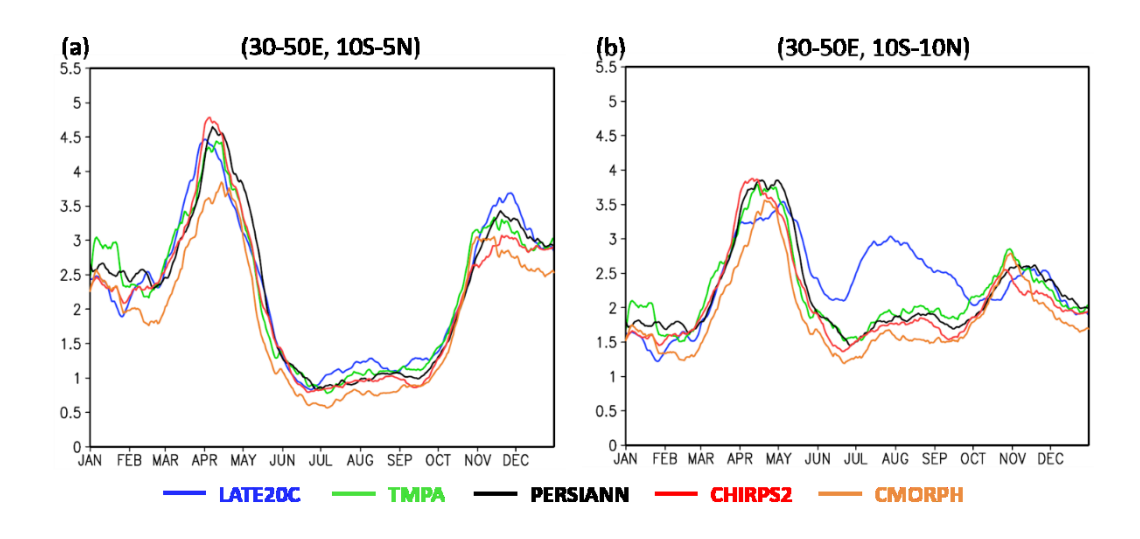


Figure 2. 20-day running mean of precipitation in the LATE20C 30-km simulations (blue), TRMM (green), CHIRPS2 (red), PERSIANN (black), and CMORPH (orange) averaged over (a) 30 to 50°E and 10S to 5°N and (b) 30 to 50°E and 10S – 10°N.

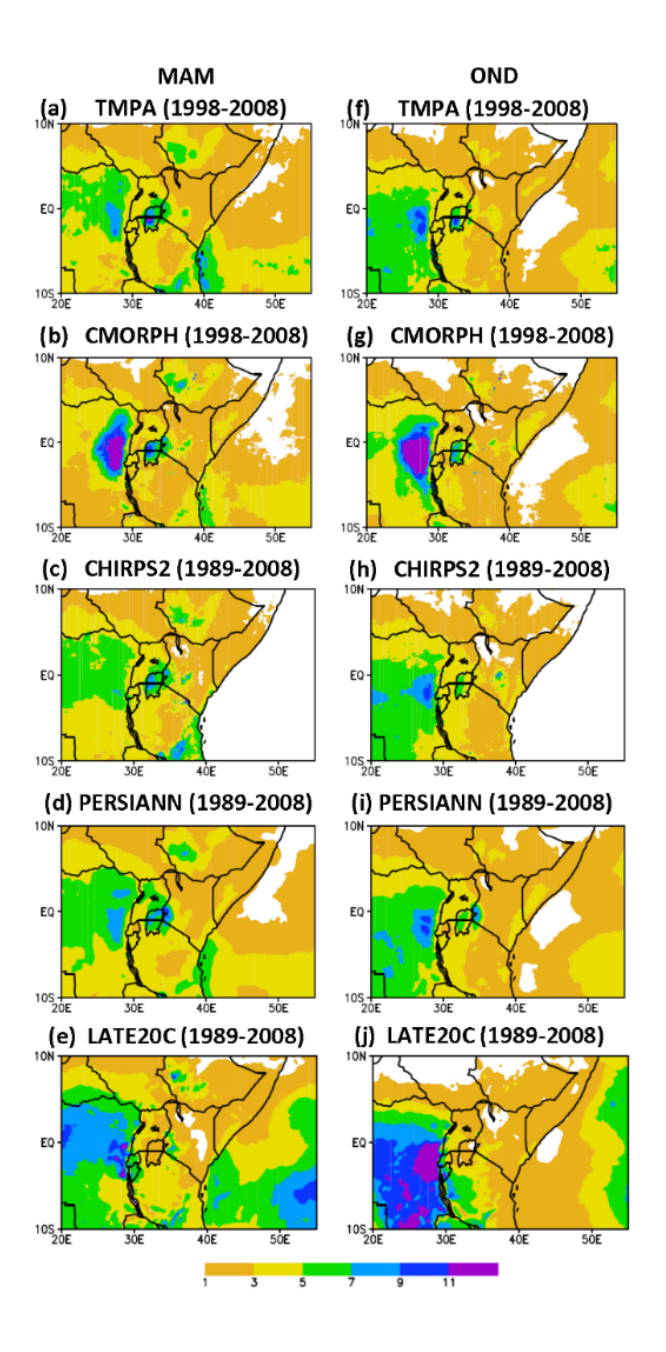


Figure 3. MAM precipitation climatologies (mm/day) from (a) TMPA, (b) CMORPH, (c) CHIRPS2, (d) PERSIANN, and (e) LATE20. OND precipitation climatologies (mm/day) from (f) TMPA, (g) CMORPH, (h) CHIRPS2, (i) PERSIANN, and (j) LATE20. Years averaged are indicated for each panel. White regions indicate rainfall rates below 1 mm/day and, in (c) and (d), missing data over the ocean.

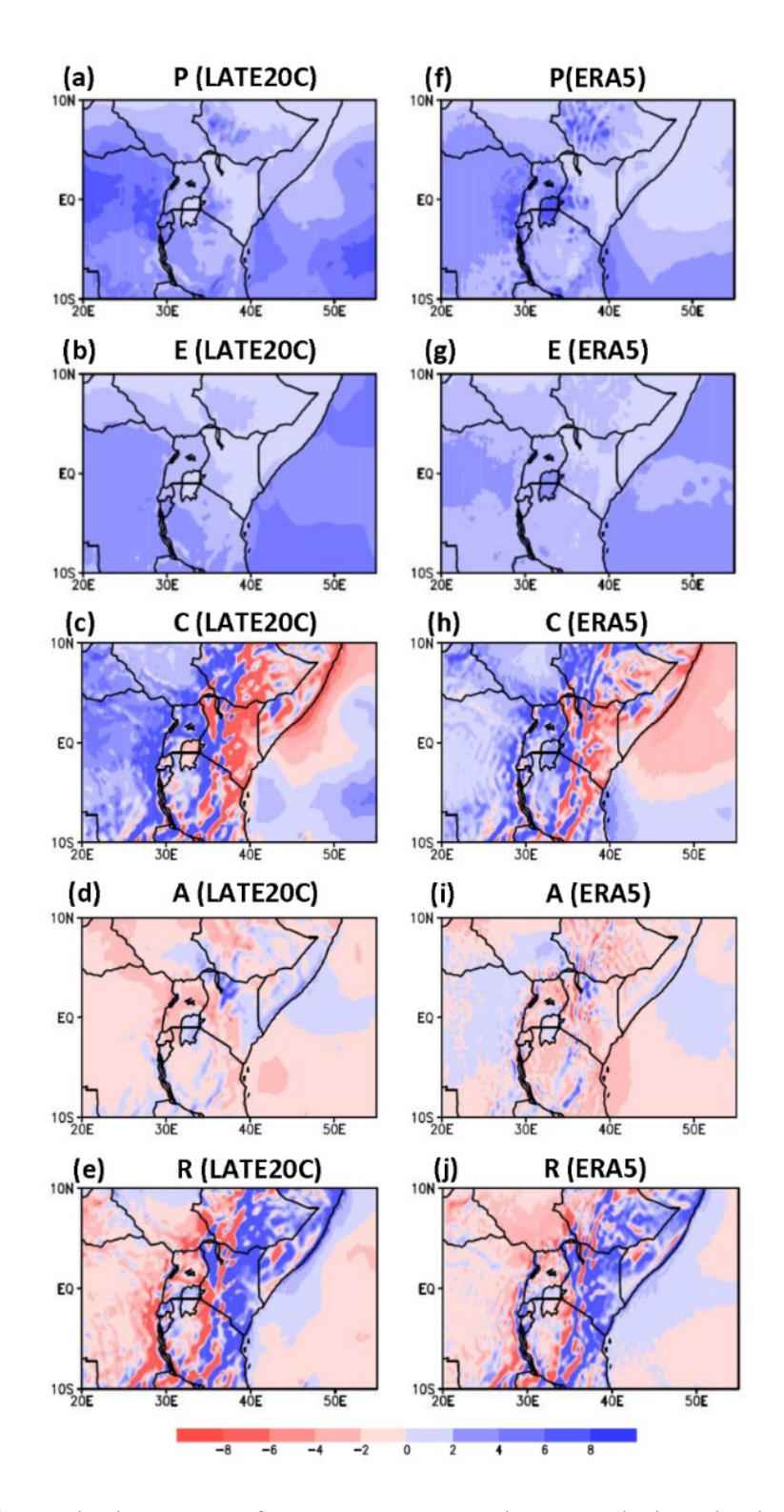


Figure 4. Moisture budget terms from LATE20C and ERA5 during the long rain months (March - May). Panels (a) - (e) display the moisture budget terms: P -precipitation (a), E - evaporation (b), C - vertically integrated moisture convergence (c), A - vertically integrated moisture advection (d), and R - residual (e), for LATE20C model output. Panels (f) - (j) are the same terms calculated in the ERA5 reanalysis.

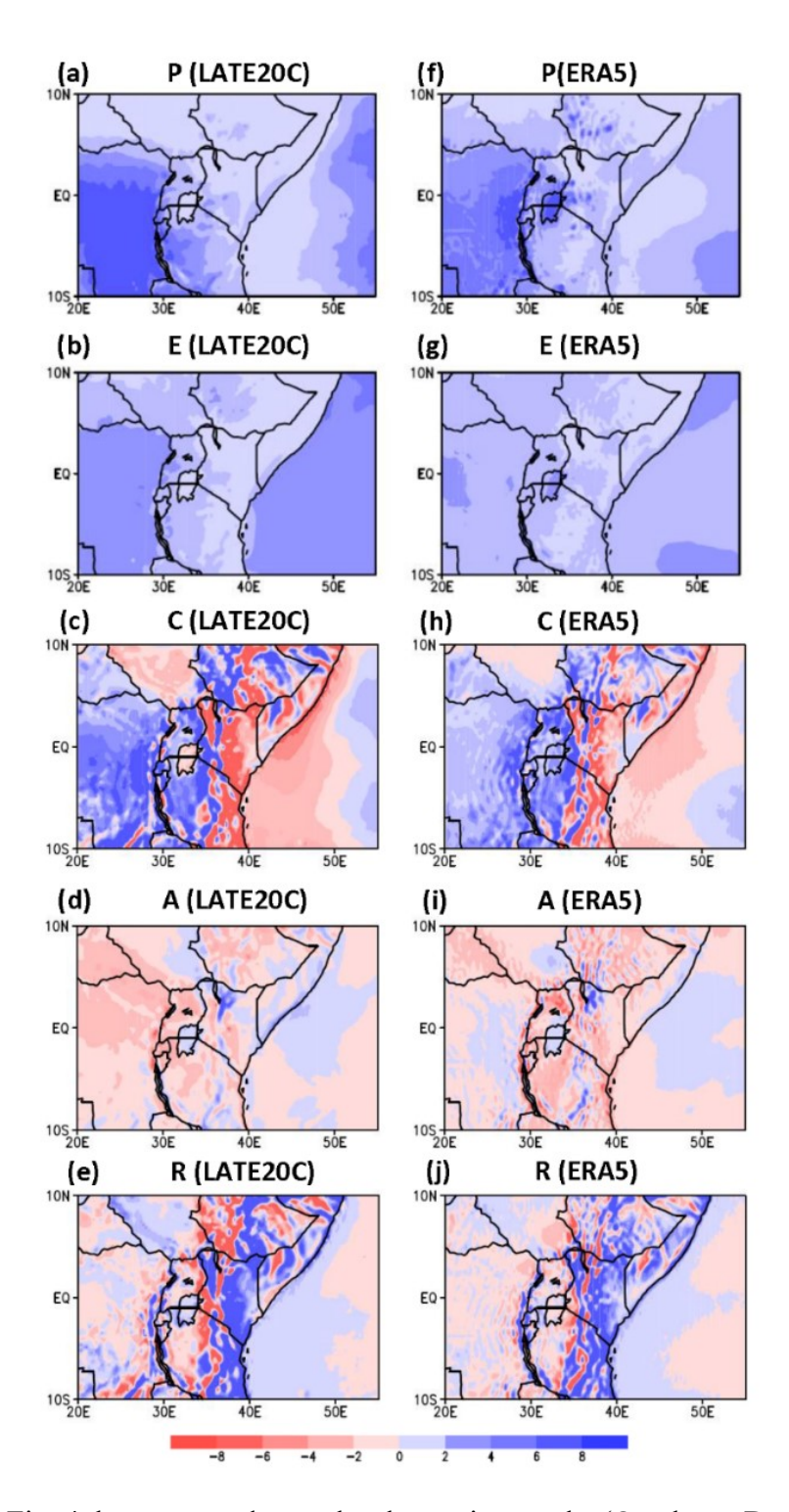


Figure 5. As in Fig. 4, but averaged over the short rain months (October – December).

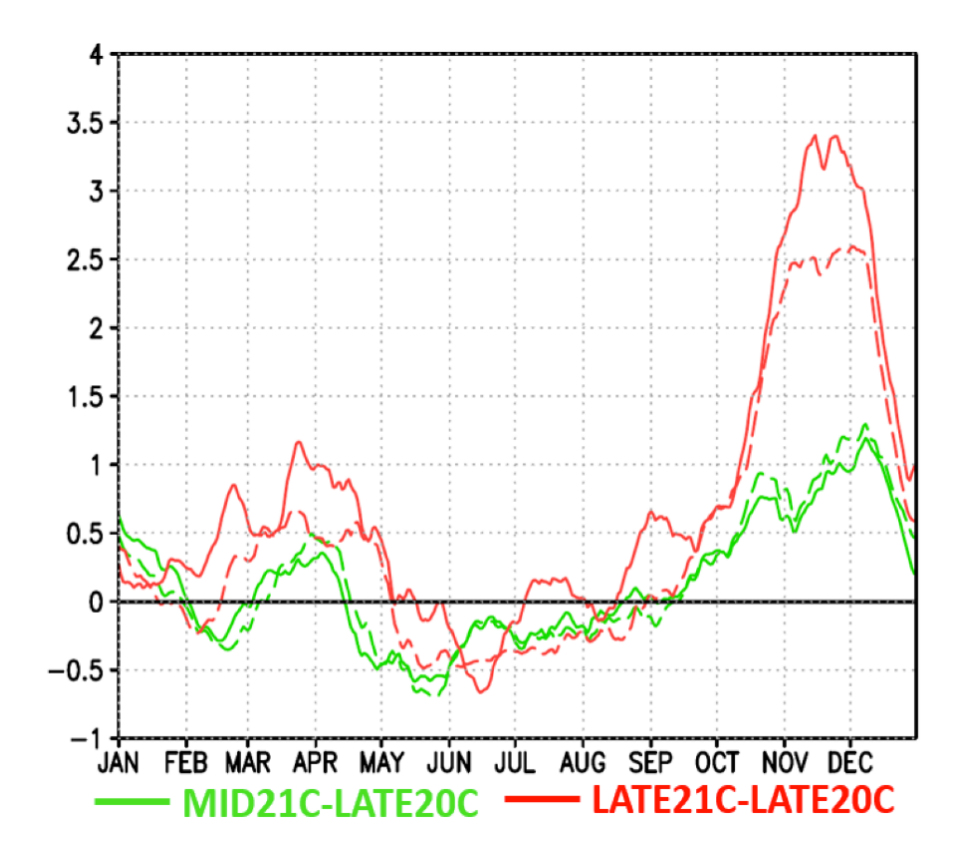


Figure 6. 20-day running mean precipitation differences for MID21C-LATE20C (green) and LATE21C-LATE20C (red) in the 30-km simulations (solid) and 90-km simulations (dashed). All values are averaged over land points from 30-50°E and 10S-10°N. Units are mm/day.

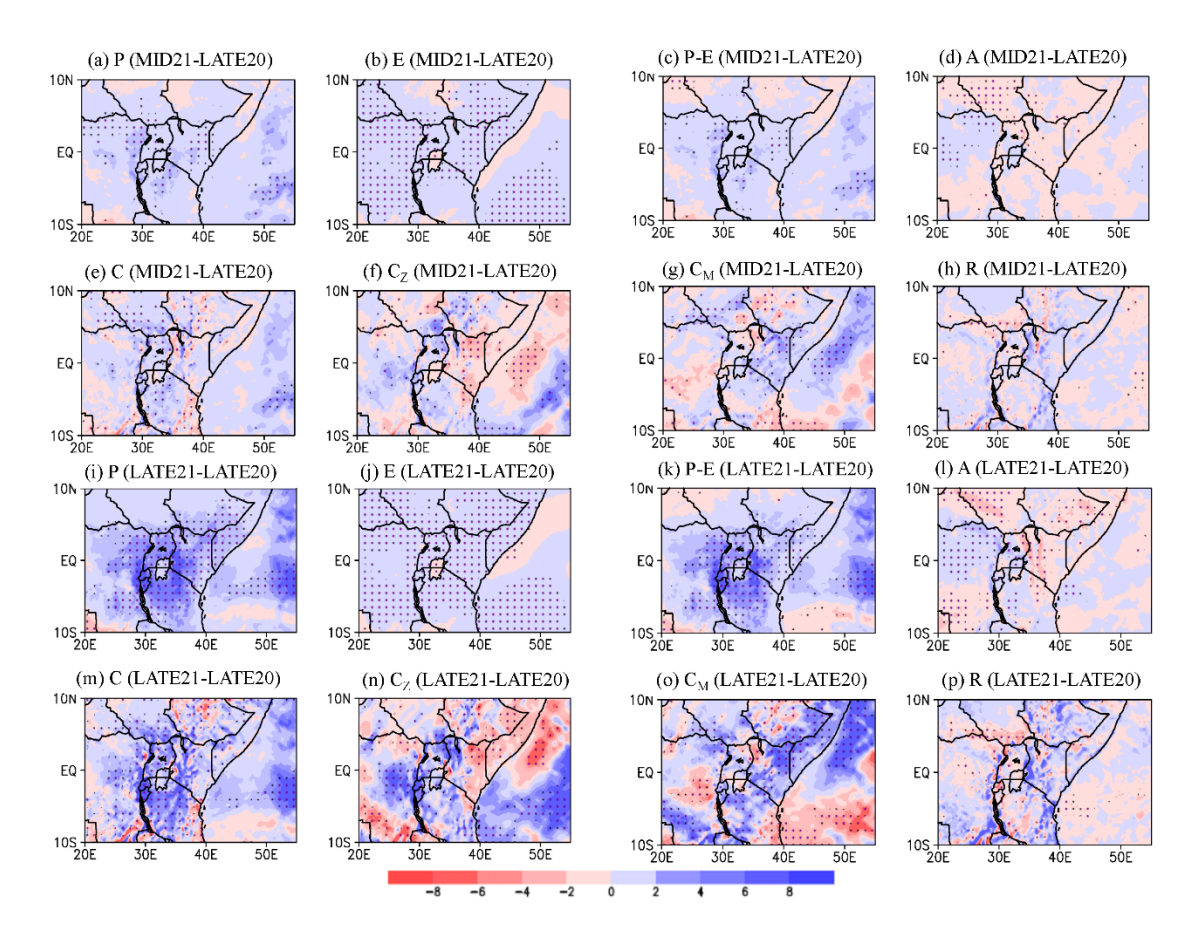


Figure 7. Differences in (a) precipitation, (b) evapotranspiration, (c) precipitation – evapotranspiration, (d) moisture advection term, (e) moisture convergence term, (f) zonal moisture convergence term, (g) meridional moisture convergence term, and (h) residual term in the moisture budget in November for MID21-LATE20. (i) - (p) are the same as (a) - (h) but for the LATE21-LATE20 differences. Units are mm/day. Black (purple) stippling denotes values that are statistically significant at the 90% (95%) confidence level.

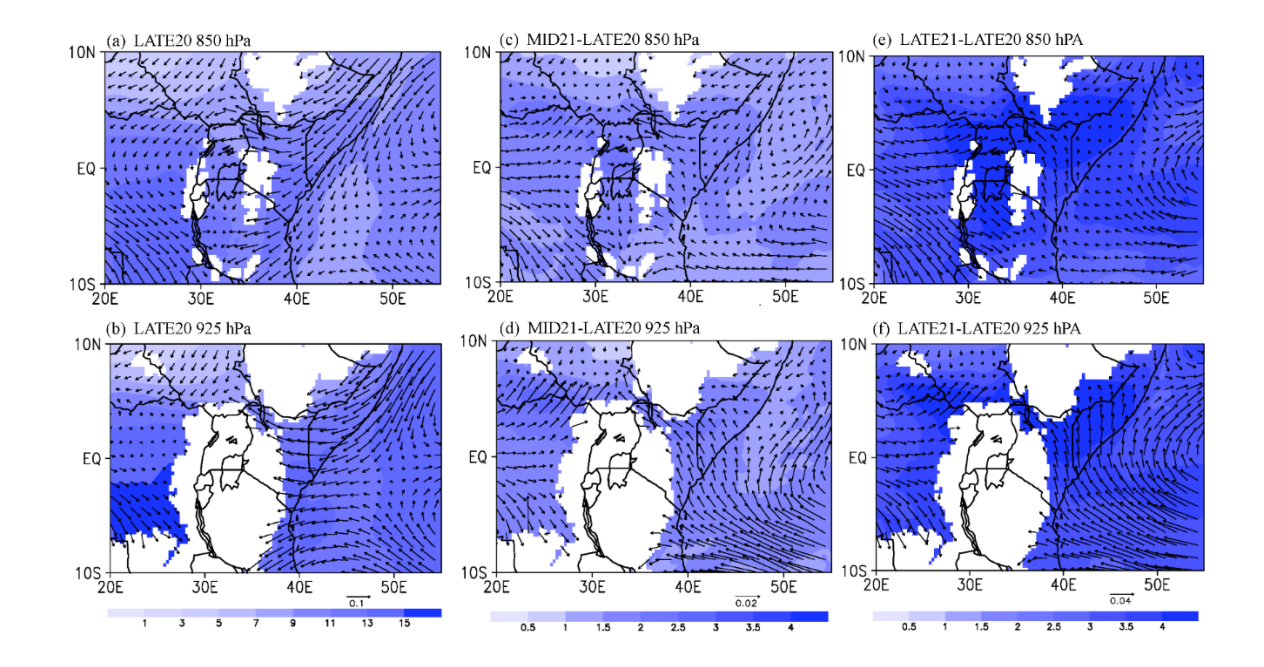


Figure 8. Climatological horizontal moisture flux (vectors; kg m kg-1 s-1) and specific humidity (g/kg) climatologies in November from the LATE20 simulation at (a) 850 hPa and (b) 925 hPa. November horizontal moisture flux (vectors; kg m kg-1 s-1) and specific humidity (g/kg) anomalies for the MID21-LATE20 difference at (c) 850 hPa and (d) 925 hPa. November horizontal moisture flux (vectors; kg m kg-1 s-1) and specific humidity (g/kg) anomalies for the LATE21-LATE20 difference at (e) 850 hPa and (f) 925 hPa. Vector scales and color bars are the same for (a) and (b), for (c) and (d), and for (e) and (f).

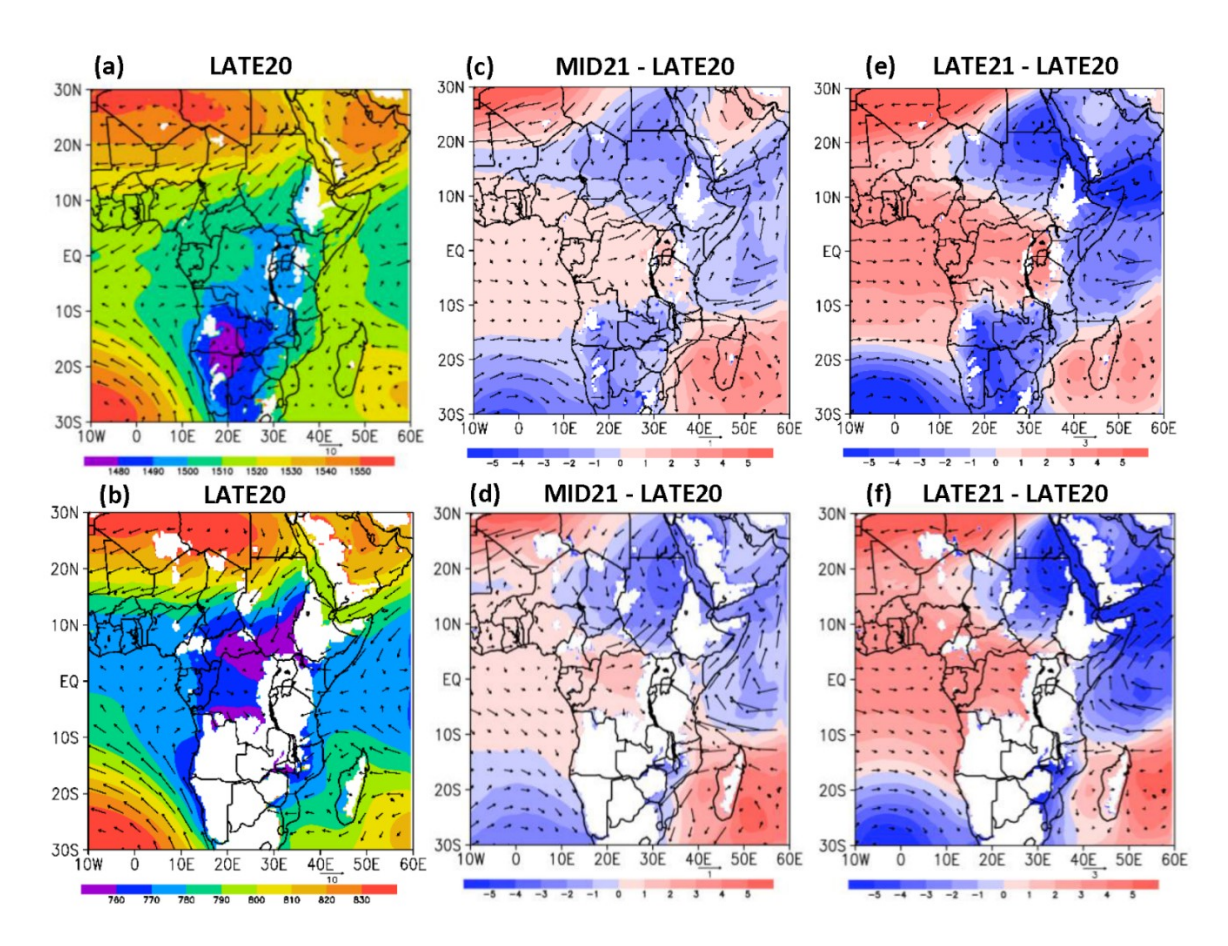


Figure 9. Climatological horizontal wind (vectors; m/s) and geopotential height (shaded; gpm) in November from the LATE20 simulation at (a) 850 hPa and (b) 925 hPa. Horizontal wind differences (vectors; m/s) and normalized geopotential height differences (shaded; gpm) in November for MID21C-LATE20C at (c) 850 hPa and (d) 925 hPa. Horizontal wind differences (vectors; m/s) and normalized geopotential height differences (shaded; gpm) in November for LATE21C-LATE20C at (e) 850 hPa and (f) 925 hPa. Topography is masked in white.

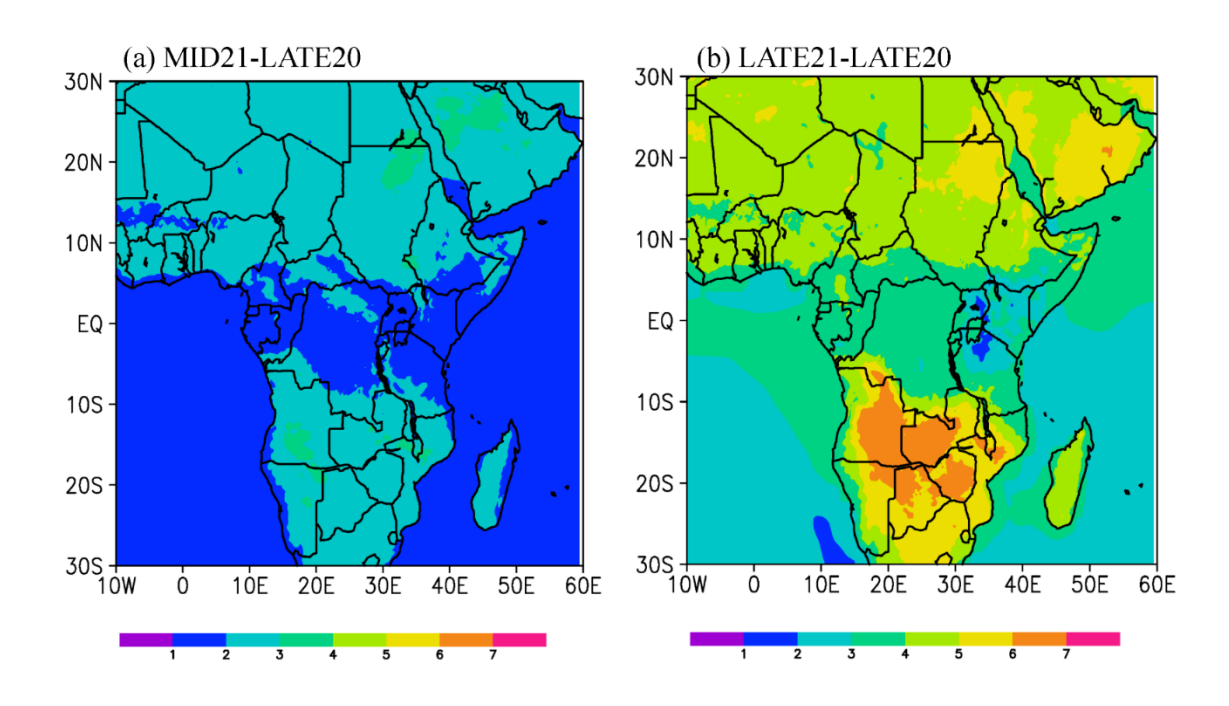


Figure 10. November surface temperature differences (K) for the (a) MID21-LATE20 and (b) LATE21-LATE20 ensemble means.

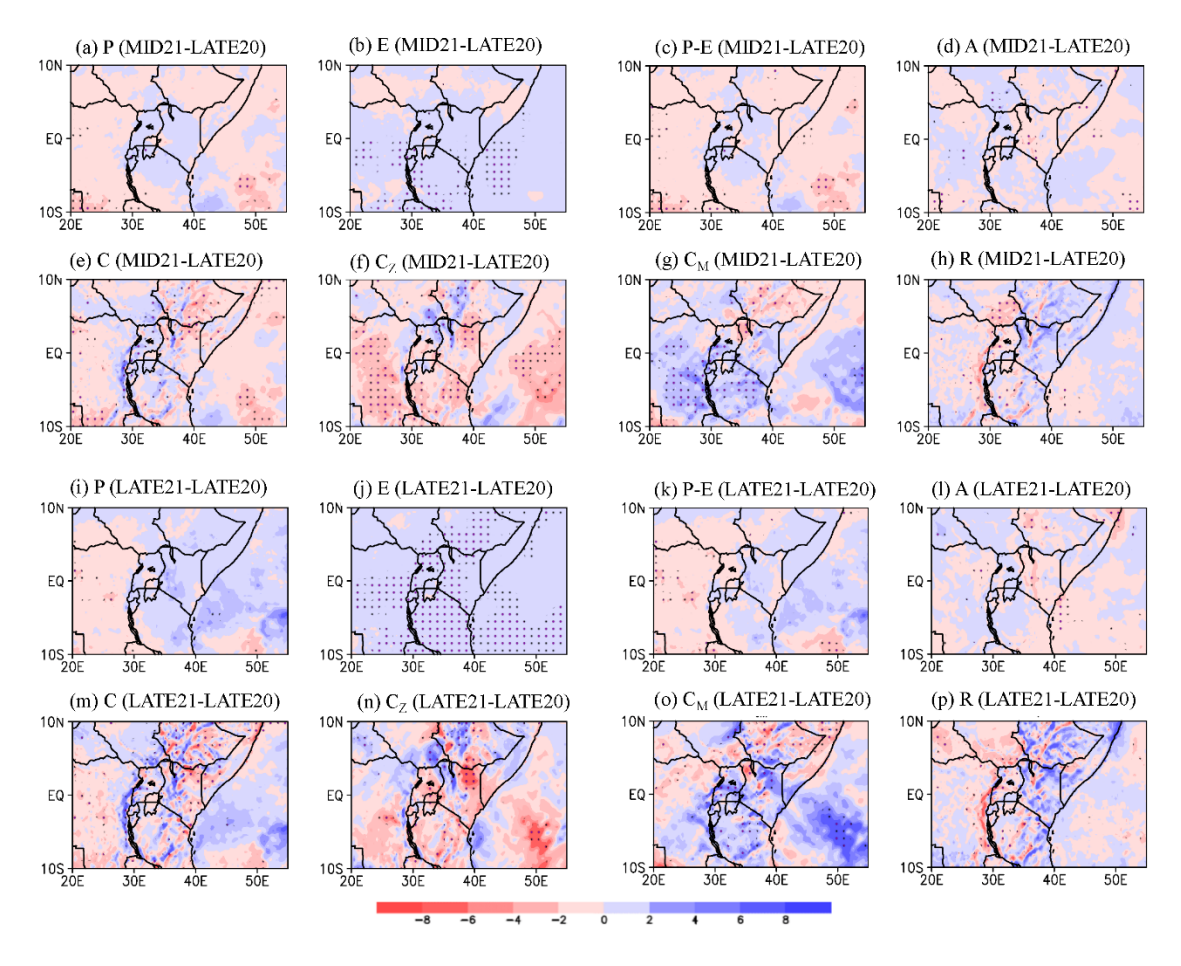


Figure 11. Differences in (a) precipitation, (b) evapotranspiration, (c) precipitation – evapotranspiration, (d) moisture advection term, (e) moisture convergence term, (f) zonal moisture convergence term, (g) meridional moisture convergence term, and (h) residual term in the moisture budget in April for MID21-LATE20. (i) - (p) are the same as (a) - (h) but for the LATE21-LATE20 differences. Units are mm/day. Black (purple) stippling denotes values that are statistically significant at the 90% (95%) confidence level.

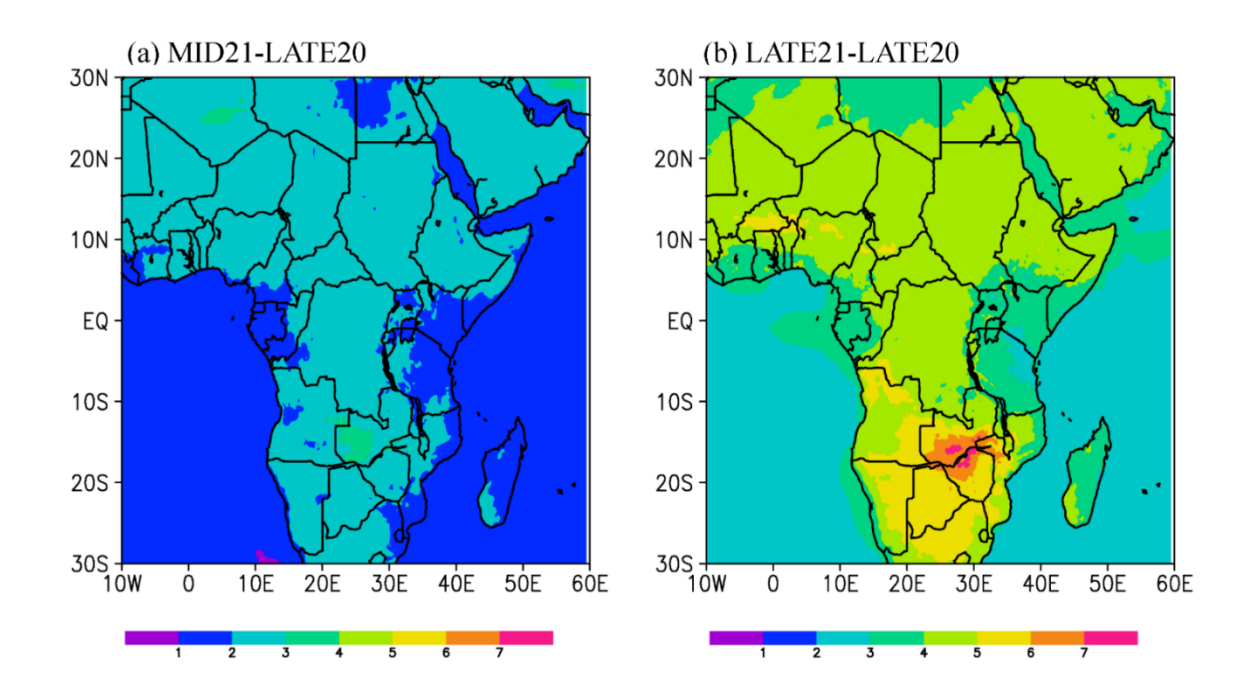


Figure 12. April surface temperature differences (K) for the (a) MID21-LATE20 and (b) LATE21-LATE20 ensemble means.

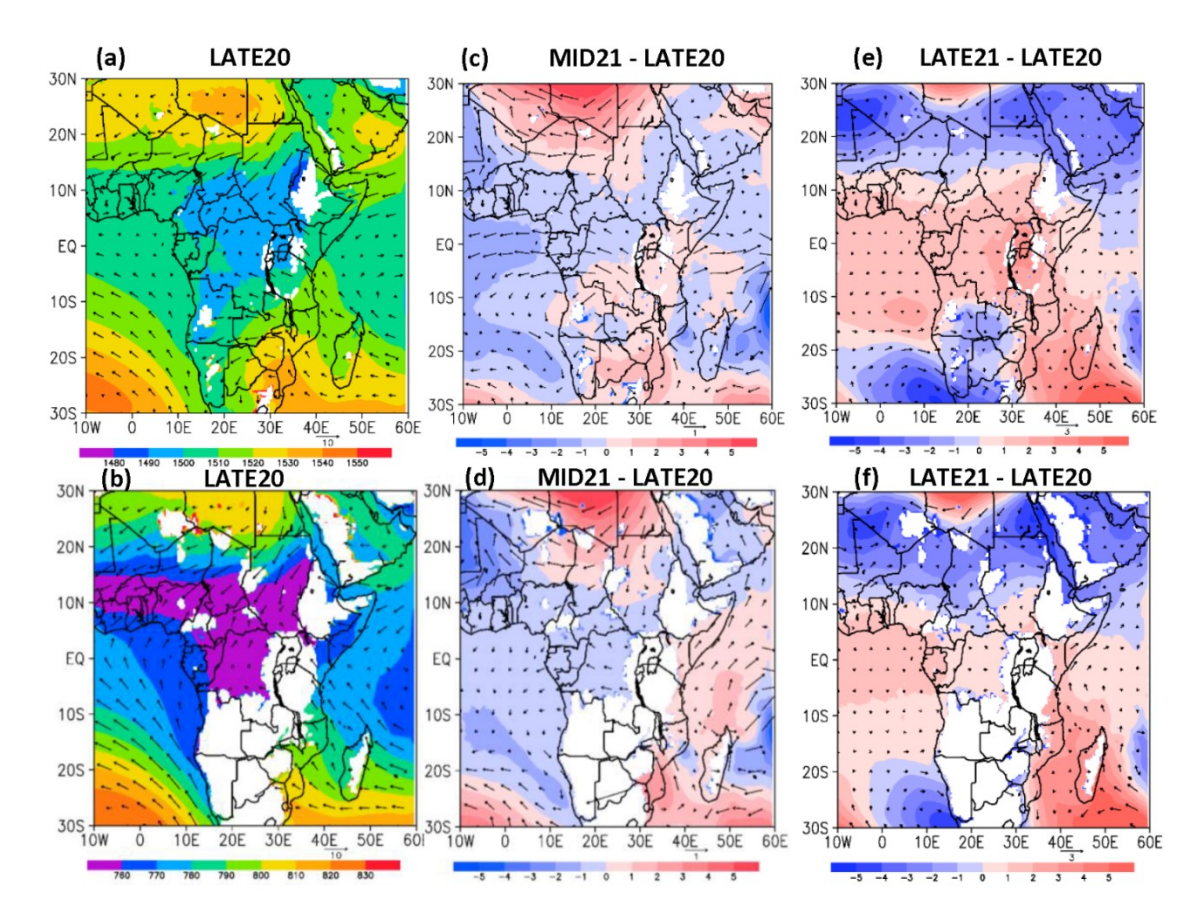


Figure 13. Climatological horizontal wind (vectors; m/s) and geopotential height (shaded; gpm) in April from the LATE20 simulation at (a) 850 hPa and (b) 925 hPa. Horizontal wind differences (vectors; m/s) and normalized geopotential height differences (shaded; gpm) in April for MID21C-LATE20C at (c) 850 hPa and (d) 925 hPa. Horizontal wind differences (vectors; m/s) and normalized geopotential height differences (shaded; gpm) in April for LATE21C-LATE20C at (e) 850 hPa and (f) 925 hPa. Topography is masked in white.